The Astrophysical Journal, 726:2 (17pp), 2011 January 1 doi:10.1088/0004-637X/726/1/2


# ASTEROSEISMOLOGY OF THE TRANSITING EXOPLANET HOST HD 17156 WITH *HUBBLE SPACE TELESCOPE* FINE GUIDANCE SENSOR*

Ronald L. Gilliland[1], Peter R. McCullough[1], Edmund P. Nelan[1], Timothy M. Brown[2], David Charbonneau[3], Philip Nutzman[3], Jørgen Christensen-Dalsgaard[4], and Hans Kjeldsen[4]
[1] Space Telescope Science Institute, 3700 San Martin Drive, Baltimore, MD 21218, USA; gillil@stsci.edu
[2] Las Cumbres Observatory Global Telescope, Goleta, CA 93117, USA
[3] Harvard-Smithsonian Center for Astrophysics, 60 Garden Street, Cambridge, MA 02138, USA
[4] Department of Physics and Astronomy, Aarhus University, DK-8000 Aarhus C, Denmark
*Received 2009 November 4; accepted 2010 October 20; published 2010 December 8*

## ABSTRACT

Observations conducted with the Fine Guidance Sensor on the *Hubble Space Telescope* (*HST*) providing high cadence and precision time-series photometry were obtained over 10 consecutive days in 2008 December on the host star of the transiting exoplanet HD 17156b. During this time, $1.0 \times 10^{12}$ photons (corrected for detector dead time) were collected in which a noise level of 163 parts per million per 30 s sum resulted, thus providing excellent sensitivity to the detection of the analog of the solar 5-minute *p*-mode oscillations. For HD 17156, robust detection of *p* modes supports the determination of the stellar mean density of $\langle\rho_*\rangle = 0.5301 \pm 0.0044$ g cm$^{-3}$ from a detailed fit to the observed frequencies of modes of degree $l = 0$, 1, and 2. This is the first star for which the direct determination of $\langle\rho_*\rangle$ has been possible using both asteroseismology and detailed analysis of a transiting planet light curve. Using the density constraint from asteroseismology, and stellar evolution modeling results in $M_* = 1.285 \pm 0.026\, M_\odot$, $R_* = 1.507 \pm 0.012\, R_\odot$, and a stellar age of $3.2 \pm 0.3$ Gyr.

*Key words:* planetary systems – stars: individual (HD 17156) – stars: oscillations – techniques: photometric

## 1. INTRODUCTION

General knowledge of stellar structure and evolution for normal main-sequence stars has long been a mature topic, with forefront research driven by increasingly precise observational constraints, and theoretical investigations including effects such as heavy element diffusion and overshoot of material at convection zone boundaries. Transiting planets, the first of which, HD 209458, was discovered only a decade ago (Charbonneau et al. 2000; Henry et al. 2000), have provided a wealth of detailed physical information about dozens of planets. Of more relevance to the current paper, high-quality transit light curves also return a direct determination of the mean density of the host star, $\langle\rho_*\rangle$, independent of stellar evolution models (e.g., Seager & Mallén-Omelas 2003; Sozzetti et al. 2007; Winn 2008). Asteroseismology has long promised fundamentally new and precise constraints on stellar structure and evolution (e.g., see the review of Brown & Gilliland 1994), and with the use of state-of-the-art ground-based spectroscopic radial velocities prompted largely by the burgeoning efforts for radial velocity (RV) planet discovery has delivered several successes in recent years (e.g., see the review of Bedding & Kjeldsen 2008). The advent of space-based photometric missions promises to provide robust results from oscillations on a much larger number of stars, as hinted at by the early successes from *CoRoT* (Michel et al. 2008). Detection of several low-angular-degree *p* modes also provides a direct constraint on $\langle\rho_*\rangle$ as will be discussed at length for HD 17156 herein.

In this paper, we present photometry of the host for the unusually interesting exoplanet HD 17156b given its long orbital period of 21.2 days discovered by Fischer et al. (2007) in a Doppler survey, and shown to have transits by Barbieri et al. (2007). The nearly 10 days of high-precision *Hubble Space Telescope* (*HST*) photometry suffices to obtain secure detection of some eight individual *p* modes, an accurate determination of the asteroseismic large separation, and hence accurate measure of the stellar mean density. A companion paper by Nutzman et al. (2011) will present analyses of complementary *HST* observations through three separate transits of HD 17156b to fix $\langle\rho_*\rangle$ from transit light curve analysis. This provides the first instance of obtaining such precise measures of this fundamental stellar parameter from two entirely different techniques, thus providing not only the intrinsically interesting physical measurement and associated interpretations, but also a test of the two methods. We find a gratifying level of consistency from independent application of the two techniques, thus providing enhanced confidence that both perform as expected.

Selection of HD 17156 as the target and the observations obtained for the asteroseismology part of this project are discussed in Section 2. Extensive, and unique, procedures invoked for the analysis of *HST* Fine Guidance Sensor (FGS) time-series photometry are discussed in Section 3. The evidence for and detailed results of power spectral and related analyses for stellar oscillations are covered in Section 4. Section 5 presents interpretation using stellar evolution and eigenfrequency analyses. Comparisons with the transit light curve analyses are provided in Section 6 along with a look to the future prospects for similar results on a much larger number of systems from the *Kepler Mission*.

## 2. TARGET CHOICE AND OBSERVATIONS

### 2.1. Target Choice and Background on FGS Use for Photometry

The underlying motivation of this study, anticipated for years in application with the *Kepler Mission*, was to simultaneously challenge the two relatively new techniques of transit light curve analysis and asteroseismology by comparing results for

* Based on observations with the NASA/ESA *Hubble Space Telescope*, obtained at the Space Telescope Science Institute, which is operated by AURA, Inc., under NASA contract NAS 5-26555.

$\langle\rho_*\rangle$ on the same object, while at the same time providing a new benchmark of accuracy for stellar and planetary quantities. Application of asteroseismology, with well-posed observations, promises determinations of stellar density to <1%, and ages to <10%—very desirable constraints on stellar structure and evolution. However, to reach such results requires a large allocation of observing time, both to reach the necessary precisions of better than a meter per second if through radial velocities, or near 1 part-per-million (ppm) if through broadband photometry, and to reach the necessary frequency resolution of order 1 $\mu$Hz. For photometry these constraints essentially come down to requiring that of order $10^{12}$ photons be collected over a period spanning about 10 days, and for which near Poisson limited results can be maintained. The best ground-based attempt with photometry to date involved using a longitude-distributed network of 4 m telescopes for a one week period in 1992 (Gilliland et al. 1993) to find oscillations in a cluster of slightly evolved stars expected to have favorable amplitudes of a few times solar; although a technical success, this study failed to detect oscillations. The capability of *HST* to provide successful asteroseismology of solar-like stars has long been expected to hold, but the necessity of dedicating 10 days of observations to one bright star has not supported successful applications. In the fall of 2008 *HST* had lost the use of its primary instruments, Advanced Camera for Surveys, NICMOS, and Space Telescope Imaging Spectrograph, leaving only the imager WFPC2 with nearly 15 yr on-orbit in service. In addition, Side A of the *HST* electronics communication package required to utilize WFPC2 failed, thus precipitating a delay in the much anticipated recent servicing mission to upgrade *Hubble*'s instruments. When use of Side B did not initially succeed, we submitted this program to allow good use of the remaining science capability of *HST* at that time: the FGSs (Nelan et al. 2008). The FGS can provide exquisite interferometric position determinations, and time-series photometry through summing the counts of the four photomultipliers (PMTs) on each FGS in the POSition mode, as well as high angular resolution, narrow field interferometry with TRANSfer mode observations; see Nelan et al. (2008) for in-depth discussion of general FGS capabilities.

Our application for DD time on *HST* was granted as GO/DD-11945, "Asteroseismology of Extrasolar Planet Host Stars." Our photometric requirements from the FGS exceeded those reached in its previous use, which usually involved single-orbit visits timed to coincide with ingress or egress of planet transits (Wittenmyer et al. 2005; Bean et al. 2008). Extensive experience has shown with other instruments on *HST* that during the first orbit, as the spacecraft thermally adjusts at a new orientation, photometric stability is much lower than in successive orbits. We were initially granted a test block of eight contiguous orbits to coincide with a transit of HD 17156b. As we expected, after the first orbit much better stability followed and these observations are discussed and used in Nutzman et al. (2011). With this successful demonstration of FGS capability, we were granted the 150 orbits necessary to follow HD 17156 for 10 days during which it was in the Continuous Viewing Zone (CVZ) of *HST* for much of this time.

The choice of HD 17156 as a target followed from a review of all 42 then known transiting planet host stars to see which would hold the best prospect of asteroseismology with a 10 day block of dedicated *HST* time with FGS. Adopting stellar parameters from Frederic Pont's table at http://www.inscience.ch/transits (no longer active—the equivalent, albeit updated information may be found at http://exoplanet.eu) and scalings for expected oscillation properties (Kjeldsen & Bedding 1995) resulted in a prediction of amplitudes at 6.9 ppm for HD 17156. With 10 days in the *HST* CVZ a signal-to-noise ratio (S/N) of $\sim 7$ was predicted for the highest amplitude modes (and ultimately close to the value reached) for these FGS observations. Since this S/N for $p$-mode detections was well above that predicted for any other transiting planet host, and the system is unusually interesting given its 21.2 day period compared to the more common 3–5 days of Hot Jupiters studied to date, the target choice was clear.

Although the discovery paper for HD 17156 appeared only three years ago, the system is now very well studied. In addition to its 21.2 day orbit, the planet has an eccentricity of 0.68. HD 17156 is one of just three transiting extrasolar planets for which Rossiter–McLaughlin radial velocity observations through transit have determined the relative stellar rotation and orbital plane alignments to good accuracy (Cochran et al. 2008; Narita et al. 2009). For HD 17156 the stellar rotation and orbit of HD 17156b are well aligned. Asteroseismology holds the promise of also providing information on the stellar rotation angle relative to the plane of the sky when rotational splitting of individual non-radial oscillation modes can be detected. For HD 17156 the Rossiter–McLaughlin study of Narita et al. (2009) fixes $v \sin i$ at $4.07 \pm 0.28$ km s$^{-1}$, which coupled with the estimate of 1.45 $R_\odot$ for HD 17156 (Winn et al. 2009) leads to an estimate of the stellar rotation period of $18.6 \pm 1.4$ days. Since our observations span only half the expected rotation period, rotational splitting of non-radial mode frequencies will remain under our frequency resolution. (In principle, the full splitting for $l = 2$, $m = \pm 2$ modes could be oversampled by a factor of 2 with our window, but our marginal S/N seems unlikely to support such higher order interpretations.) HD 17156 has been well studied spectroscopically (Fischer et al. 2007; Ammler-von Eiff et al. 2009), via transit light curve studies that determine stellar density, and augmented with stellar evolution comparisons, the stellar mass, and radius separately (e.g., see most recent such study by Winn et al. 2009), and has a parallax from *Hipparcos* with a relative error of only 5% (van Leeuwen 2007). Table 3 will include a summary of $T_{\rm eff}$, $\log(g)$, and [Fe/H] from the spectroscopic studies, as well as the primary results from this paper. Not only is HD 17156 the best star for these *HST* observations in a technical sense (CVZ, high count rate possible, and "large" predicted oscillation amplitudes), but it is also near the absolute top of transiting extrasolar planet hosts in terms of intrinsic scientific interest.

### 2.2. The Observations

Observations of HD 17156 with the FGS2 on *HST* were obtained for 147 contiguous *HST* orbits spanning 9.67 days over 2008 December 22–31. Use of FGS2r, which had not previously been used for science observations, and was scheduled for replacement (and now has been replaced) in servicing mission 4, was selected out of extreme caution at subjecting the photomultipliers to a summed count level of order $10^{12}$ photons as would follow for this $V = 8.172$ star, since some level of lost sensitivity is expected proportional to total source exposure. In the end these observations were measured to have reduced the FGS2r sensitivity by a quite acceptable level of 0.2%–0.3%, suggesting that the better calibrated FGSs could have been safely used. HD 17156 is only 0.6 mag fainter than the level at which the FGS2r digital count registers would saturate,

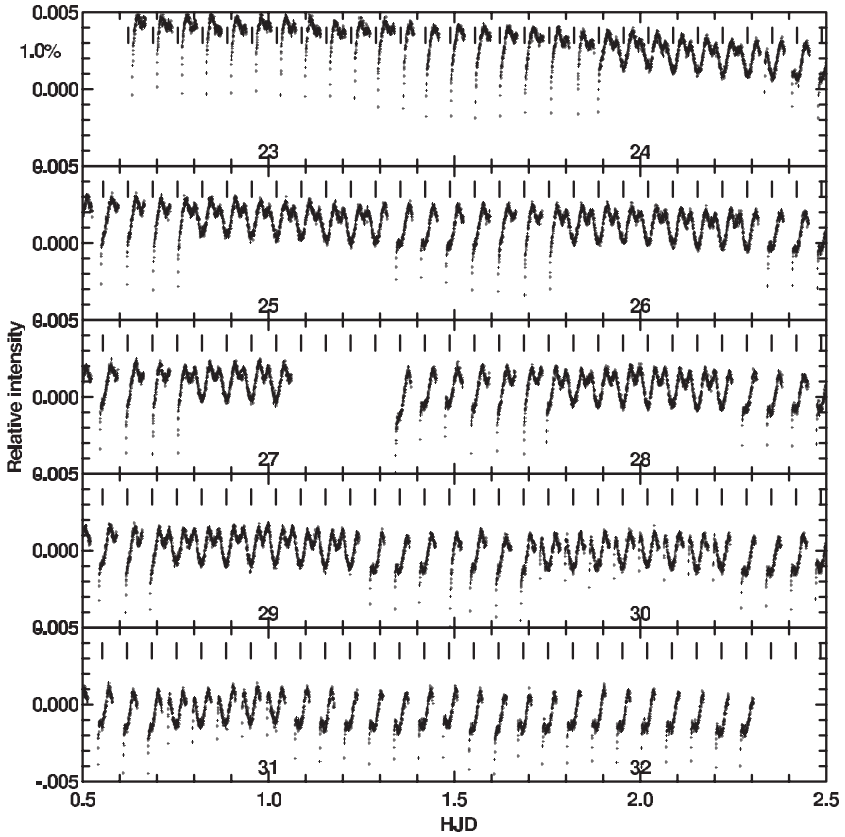


**Figure 1.** Time-series photometry for 30 s sums over the full 10 days with 2 days per panel shown starting at the top and progressing to the bottom. The numbers within the panels show start values for HJD days 23–32 (−2454800). Each panel has the same 1.0% full range, which to help guide the eye is also printed at the upper left. See the text for further details.

rendering any observations of a brighter target at full aperture impossible (Gilliland et al. 2009). Since FGS2r had not previously been used for science observations, and since none of the FGSs had been carefully calibrated for detector dead time a few additional orbits were allocated to this project for the purpose of calibrating the FGS2r dead time, background, sensitivity, and noise properties (see results in Gilliland et al. 2009).

The FGSs use photomultipliers (four in each FGS) located behind first a beam splitter based on the two senses of linear polarization, and then behind two Koesters prisms that generate an interferometric signal. The primary use of the FGSs is to track the pointing of the telescope on guide stars and provide feedback into the pointing control system. Used as a photometer in the POS mode the observing FGS (FGS2r in this case) acquires and tracks the target in fine lock, while the two guide FGSs keep the target stably positioned to start with.

The FGS data are collected at 40 Hz in each of the four PMTs per FGS. Examined at 40 Hz the relative counts from the PMTs behind each Koesters prism show strong (of order 1%) variations with characteristic timescales of about a second. The sum of the two PMTs for each polarization remains much more constant on these short timescales. We used the F583W filter covering 435–715 nm at full aperture which provides the maximum throughput available from the FGSs.

After applying a dead time correction averaging 11.0% the mean number of counts per 30 s summed over all four PMTs on HD 17156 is $4.96 \times 10^7$. Over the 9.67 days of observing, a total of 20,208 time-series points were extracted yielding a total count level of $1.00 \times 10^{12}$ photons for which an expected sensitivity limit of 1 ppm would follow if the observations are limited only by Poisson statistics.

The observations after summing over the four separate PMTs in successive blocks of 1200 samples at 40 Hz are shown in Figure 1. The data were transformed to relative photometry by dividing each sum by the global average. There are several features in the data cadence to call attention to. The *HST* orbital period often results in gaps. During the central 6 days of these observations when the target was in the CVZ for *HST* these gaps result from passing through the South Atlantic Anomaly (SAA) when high particle-event rates require the FGS photomultiplier high voltage (HV) to be shut down. Toward the start and end of the 10 days gaps also follow from occultations from the Earth as the CVZ viewing is lost. True CVZ blocks can be seen in the second through seventh days of Figure 1 with up to nine consecutive *HST* orbits of unbroken data collection. A gap occurs over HJD = 27.05–27.33 when for unknown reasons (particle hit in electronics perhaps) lock was lost and FGS2r ceased observation of HD 17156. During this 6 hr period FGS1 and FGS3 continued to track their guide stars, and FGS2 observed sky, or at least a close approximation of such about 26 arcsec from the star—this would prove useful in calibrating corrections for sky background. Time-series points for HD 17156 have only been used from periods when data quality flags show FGS2r remained in fine lock. The first data point is at HJD 22.63362 (with leading 2454800 suppressed) with the last at HJD 32.30393 for coverage of 9.67 days during which data were collected. The duty cycle (fraction of total time during which photons were usefully collected) during this interval was 72.6% reflecting the high observing efficiencies possible with *HST*. Clearly, the data structure will introduce aliases in power spectra associated with the orbital period of *HST* and the one per day cycling of CVZ periods unbroken by the SAA.

The goal of this project is to detect several independent modes of oscillation on HD 17156, the highest amplitude of which is expected to be $\leqslant$10 ppm, and to obtain an S/N of several per mode in doing so. The simply extracted time series shown in Figure 1 show peak-to-peak variations at a range of 1%, or 1000 times larger than the peak intrinsic variations expected from the star. Fortunately (and by design, we would not have attempted this otherwise), the stellar oscillations for HD 17156 are expected to have periods of 6.5–13 minutes, i.e., well separated from the bulk (but not all) of characteristic timescales reflected in the systematics apparent in Figure 1. The following section will explain the rather extreme reduction steps taken to bridge the gap between simply obtained, and necessary, noise levels in these data.

## 3. REDUCTION OF FGS2r ASTEROSEISMIC DATA

### 3.1. Removal of HST Orbital Artifacts

We have experimented with starting the data reductions using the individual 40 Hz level counts from each of the four contributing PMTs. Having found no advantages in considering the highest frequencies, we have settled on analyzing 30 s (1200 samples at 0.025 s) sums. We have also explored analyzing the pairs of PMTs separately, and again no useful utility in doing so was uncovered.

The only exception to working with 30 s sums over all four PMTs is that we have applied the dead time correction for the FGS electronics separately for each PMT at the 40 Hz level, and subtracted the relatively unimportant detector background count level of ~3 per sample per PMT (Gilliland et al. 2009). The equation adopted for dead time is (see Gilliland et al. 2009 and references therein)

$$C_T = C_M/(1.0 - C_M(T_D/T_I)), \quad (1)$$

where $C_T$ is the true number of counts within the sampling interval of $T_I = 0.025$ s, $C_M$ is the recorded number of counts in this interval, and the $T_D$ have values of 210.6, 306.0, 260.3, and 286.0 ns for the four PMTs. In a general sense, the correction for detector dead time is relatively unimportant in this paper, but essential for the analysis of transit depths since both the absolute count level and changes to that scale with this correction.

Continuing discussion of reductions by reference to Figure 1, note that after each gap in the observations there is a rapid rise in the relative intensity. The sequence within each new observation (single orbits of *HST* normally up to nine consecutive orbits when in the CVZ) is that the two guide FGSs turn on and establish "fine lock" on guide stars, and only then is the HV turned on for the science FGS and fine lock guiding established on HD 17156. This results in 40 Hz time series on HD 17156 starting at zero before HV is turned on, a rapid (~0.1 s) transition from zero to ~97% of full counts at HV turn on, and an exponential ramp up to the full count level over ~5 minutes. To facilitate correcting the data during the ~5 minutes of stabilization at the start of each observing sequence, of which we have 101 occurrences in our 10 days, the 30 s data sums are always started at the same number of 40 Hz steps after HV turn on as evidenced by rapidly rising counts. The offset between HV turn on and the start of the first 30 s sum has been chosen as 21.5 s, a somewhat arbitrary offset that puts the first 30 s sum at about 0.995 of the ultimate count rate. More on treating the ramp up of counts is provided later.

A first *HST* orbit which included brief TRANS mode observations to search for companions to HD 17156, and the start of time-series observations in the POS mode has been discarded, and is not shown in Figure 1. The TRANs mode observations show that HD 17156 appears to be a point source to the resolution of FGS2r, thus a stellar companion with a projected separation greater than about 0.015 arcsec with a $\delta V$ smaller than about 3 can be excluded. Since HD 17156 has a *Hipparcos* distance of ~78 pc (van Leeuwen 2007), 0.015 arcsec corresponds to ~1.1 AU. The published RV data do not suggest a stellar mass body with period less than a few years, so between FGS and RV, companions with $\delta V \leqslant 3$ are excluded.

A number of features are immediately obvious from inspection of Figure 1. (1) The data values trend downward by about 0.3% over the 10 days. This has been separately established to be instrumental, at least at a precision level of ~0.1% by observing the FGS standard Upgren 69 before and after the 10 days which showed a similar drop (Gilliland et al. 2009). A minor degradation of PMT sensitivity from exposure to $10^{12}$ photons was expected. (2) The *HST* orbital timescale is shown by successive vertical tick marks (95.9184 $\pm$ 0.003 minutes) to guide the eye (and later reductions). Within *HST* orbits the time series shows similar waveforms of typical full amplitude ~0.025%. These waveforms apparently evolve slowly over the 10 days. (Not shown—the two PMT pair sums show different orbital waveforms, with the variations in one being about twice the other, but both seem to show equally consistent orbit-to-orbit waveforms.) (3) At the start of each contiguous block of data the time series show a ramp up of full amplitude ~0.4% following the HV turn on.

The initial approach to data reductions, as had apparently worked quite well for the more limited (and simpler orbital waveform) data during the 2008 November 7 transit, was based on attempting decorrelations against the $x$, $y$ pointing records from all three FGSs, and the ratios of counts between PMT pairs in FGS2r itself. These are not shown; it quickly became evident that large features appear in the potential decorrelation vectors that do not appear in these times-series data over 10 days.

We will next show plots similar to Figure 1 that show several decomposition terms for the obvious artifacts. These will include in Figure 2 a minor additive correction made for varying sky background. Figure 3 will document a slow variation in time, picking up timescales that are long compared to the *HST* orbit. Figure 4 will show an *HST* orbital wave form that is allowed to evolve slowly in time. The HV ramp up in counts will be detailed in Figure 5. The factors for the slow variation in time, the orbital waveform, and the HV ramp are solved for in an iterative, least-squares procedure. Figure 6 will show a final tweak that is derived after the above iterative solution. We next detail these corrections. These corrections are applied to the raw time series such that subtraction of the Figure 2 term and a point-by-point division by the four terms from Figures 3, 4, 5, and 6 will take the raw values of Figure 1 into the corrected values of Figure 7.

#### 3.1.1. Subtraction of Sky and Particle Backgrounds

As noted in Section 2 the data gap over HJD = 27.05–27.33 proved useful for deriving a proxy for variations in the sky background. FGS1 and FGS3 both observed stars much fainter than our target HD 17156. In order to keep the bearings in the FGSs lubricated the guide FGSs were rotated between stars—FGS1 alternated between two at $V = 11.50$ and 11.53 ($\times$21.5 fainter than HD 17156) and FGS3 alternated between $V = 12.97$, 13.48, 14.31 stars ($\times$83–286 fainter than HD 17156). Changes of background occur for two reasons: (1) variations in

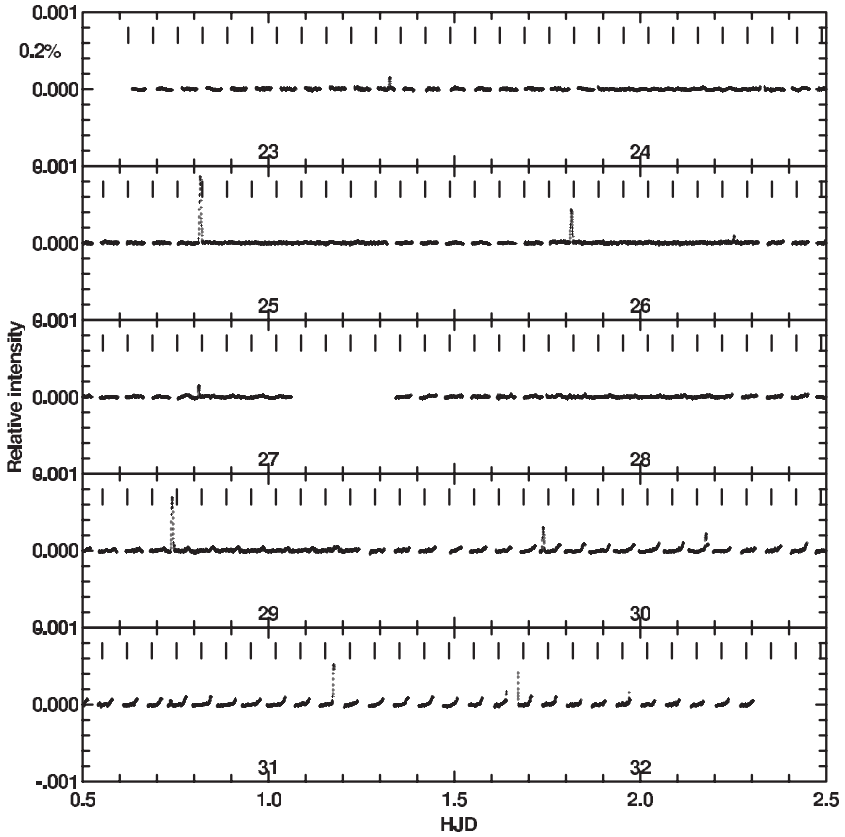


**Figure 2.** Sky plus counts from charged particles shown as corrections relative to the HD 17156 count level. See the text for how FGS1 and FGS3 counts are used as proxies for this. The sharp, positive spikes result from grazing the SAA.

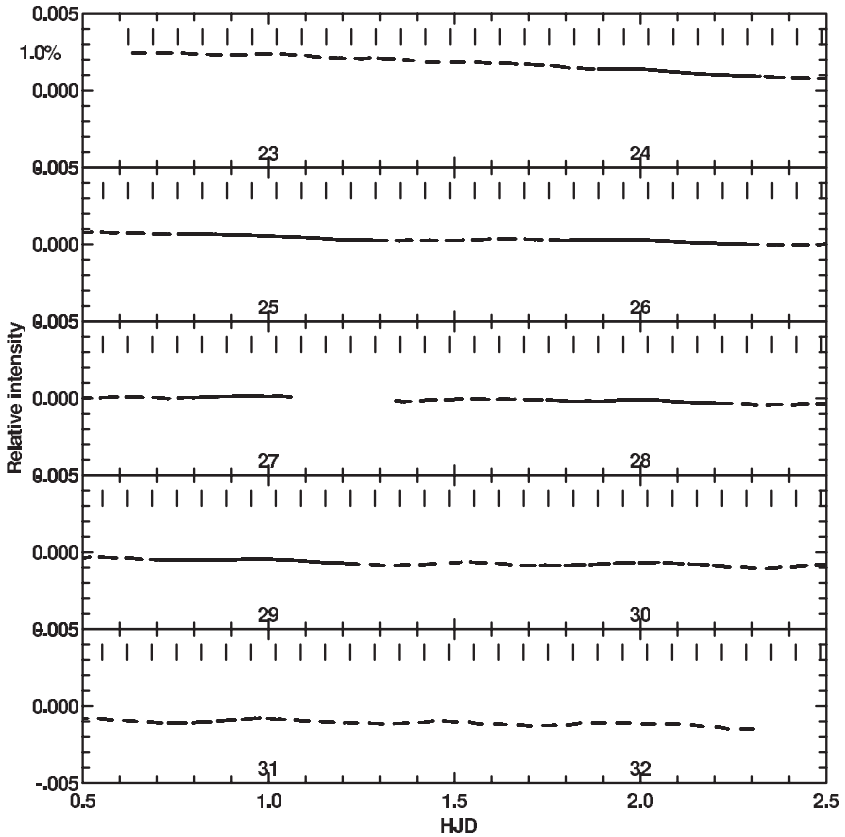


**Figure 3.** Slowly varying long-term correction factor derived by running a median filter with width of 0.15 days over the data. The 0.2%–0.3% decline overall likely follows from lost FGS PMT sensitivity, and not intrinsic variation of HD 17156.

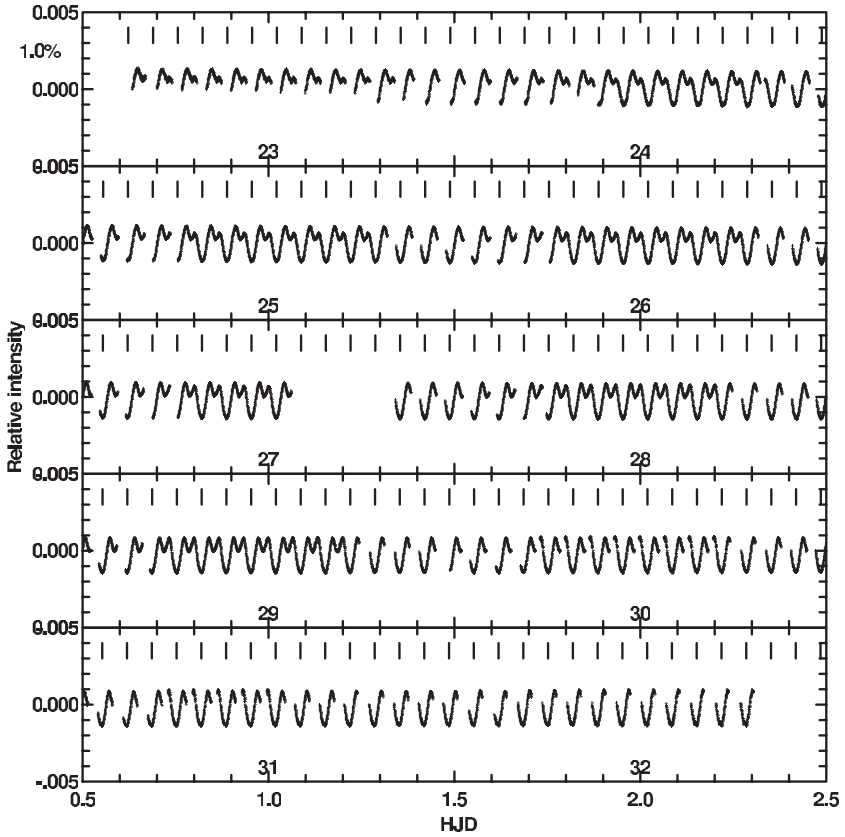


**Figure 4.** Orbital waveform component of data corrections plotted on the same times and scale of Figure 1.

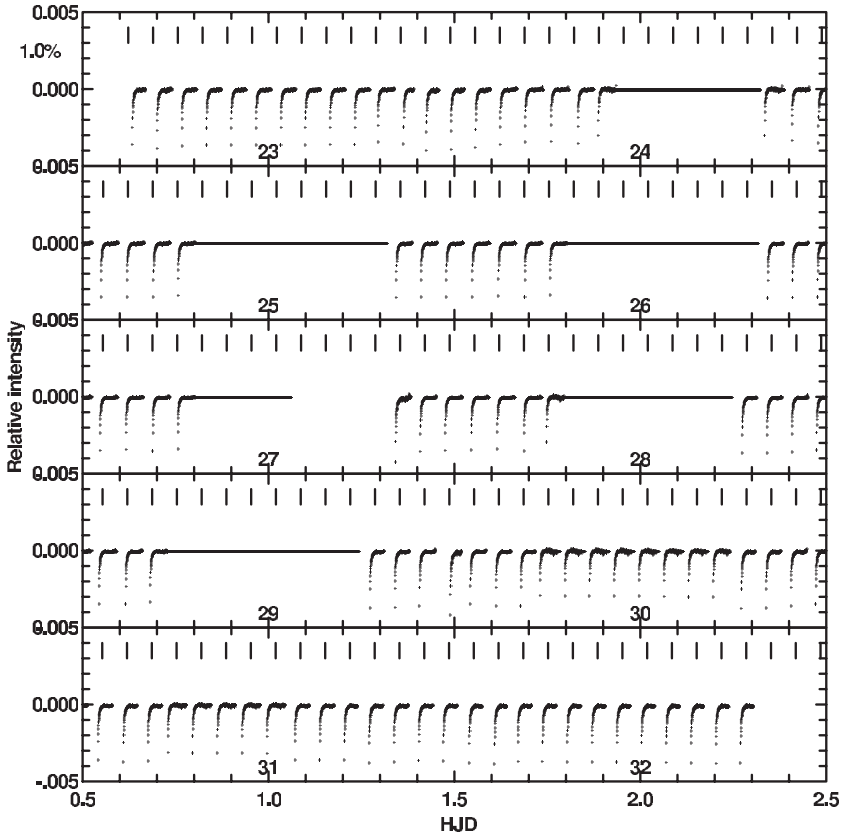


**Figure 5.** Correction factor for HV ramp up, based on a bilinear regression over the preceding time gap, and overall time for each successive point in observing sequences.

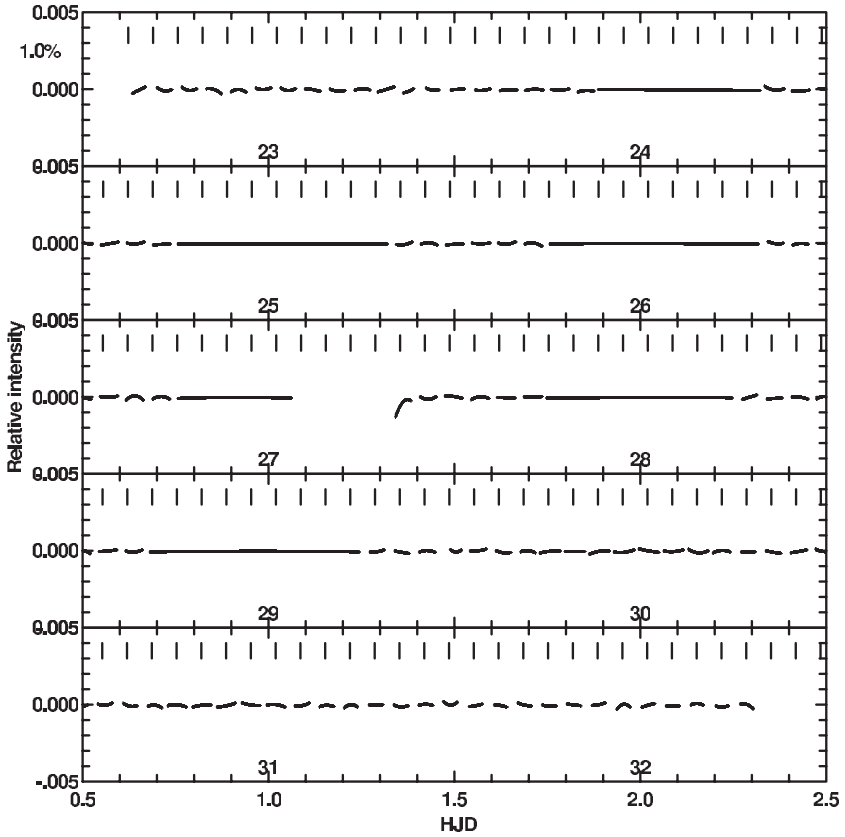


**Figure 6.** Final corrections derived after the iterative solution and application for slow-drift, orbital waveform, and HV ramp changes. The solution follows from a simple quadratic polynomial fit to each data segment.

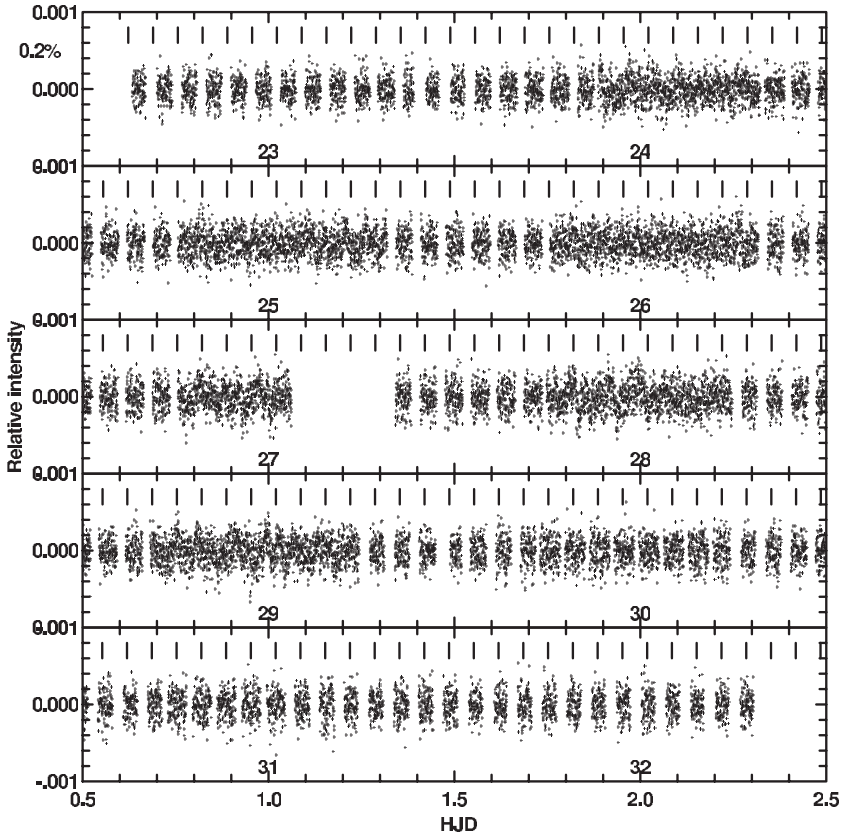


**Figure 7.** Same as Figure 1, but after having removed all of the data artifacts discussed above. Note that relative to Figure 1 the vertical plot scale has changed by a factor of 5 to a full range of 0.2%. The rms of these 30 s sums (ignoring six points deviant at more than $4\sigma$) is 163.86 ppm.

the background light, e.g., scattered from the bright Earth limb, and (2) changes in the charged particle flux inducing counts in the PMTs. Complete discussion developing FGS1 and FGS3 count rate changes as a proxy for FGS2r need not be recounted in detail here—FGS2r is no longer on the telescope and was only used for science observations for the current program. Suffice it to note that minor differences in scaling for each of FGS1 and FGS3 to FGS2r background changes exist, and these are slightly different between contributions from light and charged particle-induced counts. Also complicating this, one of the FGS1 stars was an obvious variable, but for which the intrinsic variations could be filtered out. Fortunately, the 6 hr gap while FGS2r was observing only sky provided good data for calibrating use of FGS1 and FGS3 as proxies, and the implied corrections as shown in Figure 2 are very minor for the extremely bright HD 17156. The subtraction for sky is performed before any of the more important corrections to be detailed next are developed in an iterative sense. Only the occasional brush with outer SAA regions leads to spikes that still remain under 0.09%, and these are well determined. We believe that uncertainties in the sky subtraction are quite unimportant.

#### 3.1.2. Slow Variation of Count Rate

The slowly varying count rate is shown in Figure 3 and has been derived by running a median filter of full width equal to 2.2 *HST* orbits over the data of Figure 1 (this is done only after sky subtraction and having accounted for the orbital wave form and HV ramp terms to be discussed next). This filtering should have virtually no impact on stellar oscillations for which we expect timescales of 5–15 minutes in HD 17156, while the filter is 211 minutes wide.

#### 3.1.3. HST Orbit-induced Orbital Waveform

The most interesting and important artifact in the data to be dealt with arises from highly repeatable systematics tied to the *HST* orbit. The source of these variations is treated as unknown for these purposes, and it is unknown. The orbital waveform derived from the data is shown in Figure 4. To derive this an assumed *HST* orbital phase is generated for all the data points (the *HST* orbital period is allowed to change later as needed to produce optimal results, but a good value is easily derived from inspection). The waveform is solved for on each of 1000 phase points spanning an *HST* orbit with weights set as $\exp(-(\delta t/10.4)^2)$, where $\delta t$ is the time in seconds that the center of given 30 s sums is out of phase alignment for the orbital phase point being solved for. Essentially, one makes a stack of all the data points folded on the assumed *HST* orbital period and makes a weighted average at each phase point as the ratio of the dot product of data and weights divided by the sum of the weights. In practice, this solution either does not (initially) use the points impacted by HV turn on or (later) includes these points after correction for the HV ramp. Likewise, the solution assumes the slow variation shown in Figure 3 has first been removed. The apparent slow variation in time of the orbital waveform is included by forming not a simple weighted sum at each phase point, but rather a quadratic fit over the 10 days in time. Later in the iteration cycle this is increased to fitting a cubic in time. Finally, with the orbital waveform in hand, which consists of the zero point, linear, quadratic, and cubic polynomial terms at each of 1000 phase points, interpolation is used to provide the correction at the center of each 30 s data point. We do not claim that this nested, iterative solution for the orbital waveform provides either a unique, or optimal correction. However, inspection of Figures 1 and 4 shows that the derived orbital correction does an excellent job of matching features, and thus removing the *HST*-orbit-induced systematics.

#### 3.1.4. High Voltage Ramp Up

The correction factor for the HV ramp period is shown in Figure 5. As discussed earlier each 30 s sum is initiated (to ∼0.01 s rms) at exactly the same offset following HV turn on. To first order we assume that after each HV turn on successive data points experience the same suppression of count rate. But we can do better. The offsets in successive accumulated sums after HV turn on show a strong correlation against the length of time the HV was off, equivalently the length of time the PMTs and FGS electronics were not experiencing a high photon flux. After removing the linear correlation with time gap a minor dependence on time over the 10 days is also clear. In practice the solution for each successive HV turn on point is formed as a multi-linear regression over the time gap, and time (ignoring only the case following the large 6 hr time gap which is not consistently off by this amount). This solution is followed for the first 135 points in sequences, although most of the effect is restricted to the first 5–8 minutes. Following all corrections the scatter of points near the start of observing sequences is no larger than the general scatter in the time series. The HV ramp is corrected with essentially no residual error, thus restoring some 12 hr of data that would otherwise need to be dropped since the variations in these time periods contain frequency components that would directly affect the ability to cleanly detect oscillations of 5–15 minutes.

#### 3.1.5. Residual Orbital Corrections

After having applied the several correction factors discussed above, it was clear from inspection that some obvious, albeit much smaller, residuals remained. A quadratic fit to each individual data segment has been effective in dealing with much of the residuals. Before applying this correction the overall rms had been reduced to 172.22 ppm, after applying a quadratic fit over each data segment as shown in Figure 6 the fully corrected data are shown in Figure 7. This is the time series that will be used later to form power spectra and search for evidence of $p$ modes. The time-series rms here is 163.86 ppm. The dead-time-corrected count level would imply a limit of 141.93 ppm at 30 s. Based on these numbers the removal of artifacts has provided data within 15% of the Poisson limit.

### 3.2. Effect on Power Spectrum Frequency Content

With the corrected time series in hand as shown in Figure 7, we are now ready to explore evidence for coherent oscillations. With an rms of 163.86 ppm over 20202 data points retained (dropping 6 with $4\sigma$ deviations), the noise level is expected to be 1.15 ppm globally in amplitude, likely lower and near 1.0 ppm at frequencies beyond 1.5 mHz. A power spectrum is shown in Figure 8 over 0.5–4.0 mHz. Below about 1 mHz the reduction steps discussed above, coupled with large systematics, do not provide useful information on any stellar variations. Above about 2.5 mHz inspection shows that the resulting power spectrum seems only to reflect noise. Based on published scaling relations and knowledge of the stellar parameters, we would expect oscillations peaking over 1.5–2.0 mHz at perhaps 30% higher than solar amplitude, with a large separation of some 87 $\mu$Hz. The errors on stellar parameters, in particular the mean stellar density of 0.589 g cm$^{-3}$, and −0.103, +0.066 $1\sigma$ errors

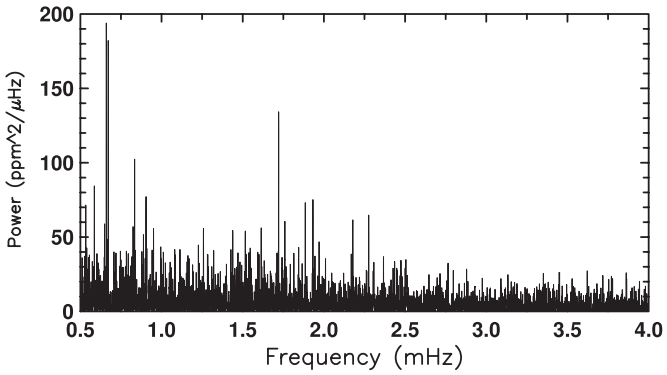


**Figure 8.** Power spectrum for the corrected data on HD 17156 as shown in Figure 7. The mean background noise level near 4 ppm$^2$ $\mu$Hz$^{-1}$ is evident above 2.5 $\mu$Hz. The spectrum below 1 mHz is likely still contaminated by systematics.

from Winn et al. (2009), project to a large separation of 87.3 $\mu$Hz with a 1$\sigma$ range of 79.3–92.0 $\mu$Hz.

The upper panel of Figure 9 shows a restricted range of 1.0–2.6 mHz for the power spectrum. A window function is shown as the middle panel in Figure 9. This was formed by generating a time series on the observed cadence with very low amplitude white noise and a large amplitude sinusoid at the same (1.7211 mHz) frequency as the highest peak in HD 17156. The most prominent sidelobes are at multiples of the *HST* orbit as expected, with smaller features reflecting the daily changes forced by SAA avoidance.

Some of our reduction steps discussed above have been rather drastic. In particular, the orbital waveform correction shown in Figure 4 will suppress any real oscillation frequencies that happen to coincide with *HST* orbital harmonics (multiples of the 173.828 $\mu$Hz orbital frequency). To quantify this we have injected a test signal of 60 ppm into the raw data (Figure 1), then performed all of the reductions detailed in Figures 2–6, following this with a new power spectrum. This is done at every frequency for which the power spectrum is evaluated. The ratio of power at the injection frequency to the input value then forms the response function shown in the bottom panel of Figure 9. As expected, signals at harmonics of the *HST* orbit are strongly suppressed. However, the portion of frequency phase space in which signal power is suppressed by more than 20% (response function <0.8) is only 4.7%. Knowledge of the response function should be taken into account in searching for evidence of *p*-mode oscillations. The response function is fixed in frequency, while of course the sidelobes of the window function shift in concert with source mode frequencies.

## 4. EVIDENCE FOR STELLAR OSCILLATIONS

The asteroseismic analysis of the HD 17156 data has been performed using the pipeline developed at the Kepler Asteroseismic Science Operations Center as described in Christensen-Dalsgaard et al. (2008). A more extended discussion of Kepler pipeline analysis tools can be found in Huber et al. (2009). The outline of analysis steps follows. (1) Calculation of the power spectrum. (2) Application of a matched filter (modified approach differing from, but with similarities to the usual comb filter) method to determine the large frequency separation. (3) Calculate the folded power spectrum using the large frequency separation. (4) Identify relation of $l$ mode frequencies

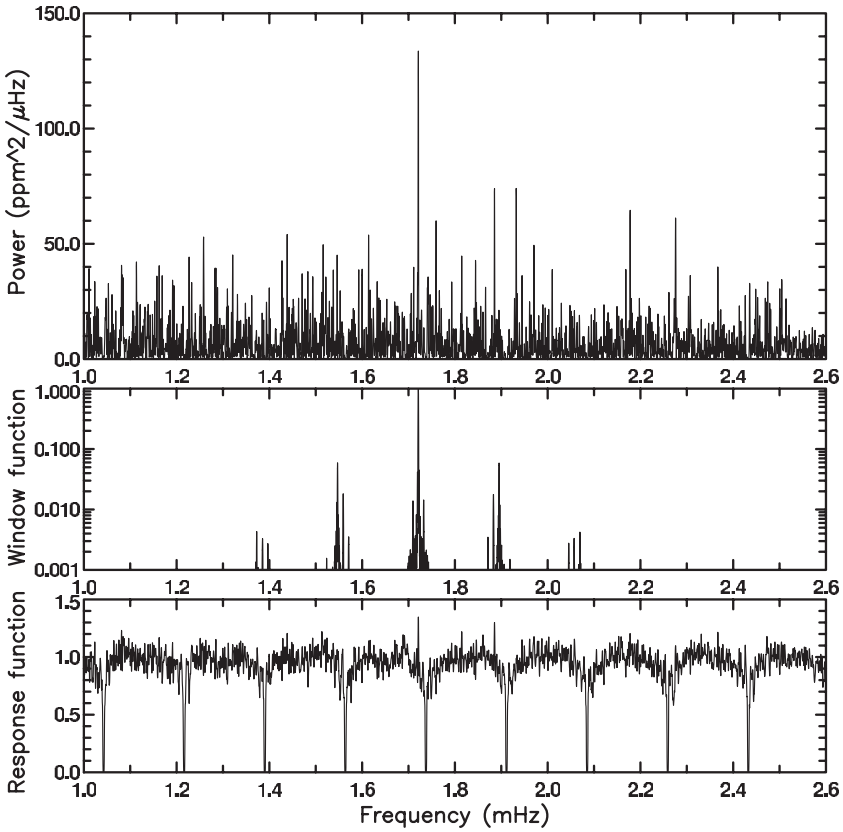


**Figure 9.** Upper panel shows the power spectrum over a restricted range of 1.0–2.6 mHz. The adopted frequency resolution of 0.25 $\mu$Hz oversamples by about a factor of 5. The middle panel shows the window function for the power spectrum from injecting a strong sinusoid at the times of observations at the frequency of the strongest peak in the upper panel. The lower panel shows the response, or transfer function of the data reduction procedure used in removing artifacts from these data.

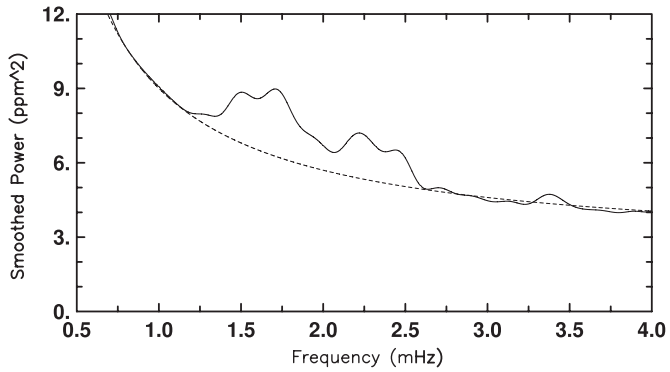


**Figure 10.** Smoothed power spectrum for HD 17156 shown as the solid line with a fit to the background from frequencies over 0.5 to 1.2 and above 2.6 mHz shown as a dashed line. The power excess of modes over 1.3–2.4 mHz in the expected domain for oscillations on HD 17156 is clear.

relative to the large separation. (5) Derivation of individual frequencies and fit to the asymptotic relation. (6) Calculation of the oscillation amplitudes corresponding to the radial, $l = 0$ modes.

Oscillation frequencies for low-degree, $p$ modes are well approximated by a regular series of peaks for which the oscillation frequencies are given by the approximate asymptotic relation:

$$\nu_{nl} \approx \Delta\nu_0(n + l/2 + \epsilon) - D_0 l(l+1), \quad (2)$$

where $\Delta\nu_0 = (2\int_0^R dr/c)^{-1}$ corresponds to the inverse of the sound travel time across the stellar diameter, and closely relates to the stellar mean density via

$$\Delta\nu_0 \approx 135(M_*/R_*^3)^{1/2}\,\mu\text{Hz}, \quad (3)$$

where $M_*$ and $R_*$ are the stellar mass and radius in solar units, and the large separation for the Sun is approximately 135 $\mu$Hz.

In the above equations, $n$ is the radial order and $l$ the angular degree of trapped oscillation modes. $D_0$ is sensitive to the sound speed near the stellar core and $\epsilon$ is a correction factor absorbing minor frequency-dependent corrections sensitive to the stellar surface layers. A recent review of the theory of solar-like oscillations may be found in Christensen-Dalsgaard (2004).

Although individual peaks may be visible in the power spectrum first shown in Figure 8, guided by an expectation given the scaling relations of Kjeldsen & Bedding (1995) for largest amplitudes of about 7 ppm near 1.65 mHz, these results are in a low S/N regime in which reliance on the existence of evenly spaced peaks in frequency must be an inherent part of the process of coaxing information on the oscillations from the data.

A smoothed version of the power spectrum is illustrated in Figure 10 which clearly shows the excess of power for HD 17156. The philosophy behind this analysis is developed in order to avoid the stochastic nature of the excitation and damping of individual oscillation modes. In order to measure the oscillation amplitude in a way that is independent of these effects, Kjeldsen et al. (2005, 2008b) have suggested a method that involves heavily smoothing the power spectrum in order to produce a single hump of excess power that is insensitive to the fact that the oscillation spectrum has discrete peaks. Following Kjeldsen et al. (2008b), we smoothed the power spectrum by convolving (in power) with a Gaussian having an FWHM of four times the large separation.

Following Christensen-Dalsgaard et al. (2008) and Huber et al. (2009), we first determine the value of the large separation

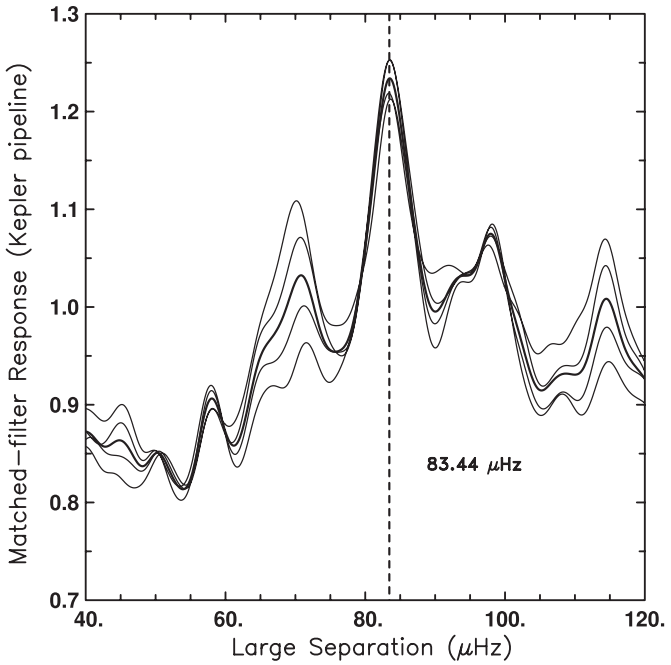


**Figure 11.** Matched filter-response function showing the large separation $\Delta\nu_0$ for HD 17156. The curves show results of individual foldings of the spectra using $n_0 = 19.5, 20, \ldots, 21.5$. At 40 $\mu$Hz the search range is $860 \pm 200$ $\mu$Hz, while at 120 $\mu$Hz the range is $2580 \pm 600$ $\mu$Hz. The more precisely determined value from fits of individual frequencies to the asymptotic relation is shown at 83.44 $\mu$Hz with the dashed line.

that best fits the power spectrum, as was outlined by Christensen-Dalsgaard et al. (2007). The idea is to match to the power spectrum a series of peaks described such that they follow the asymptotic relation (Equation (2)). To suppress the effect of the last term in that equation (giving rise to the so-called small frequency separation; see below) and avoid being sensitive to the small deviations from the asymptotic description, the analysis is carried out for a smoothed power spectrum $\bar{P}(\nu)$. Specifically, this is obtained from the original power spectrum through Gaussian smoothing with an FWHM of 3 $\mu$Hz. We now sum the power at uniformly spaced frequencies $\nu_k = \Delta\nu(k/2 + \epsilon_0)$ corresponding to the leading-order asymptotic expression, by calculating

$$\mathcal{F}(\Delta\nu, \epsilon_0) = \sum_{k=2n_0-\Delta k}^{2n_0-\Delta k} \bar{P}(\nu_k) \quad (4)$$

as a function of trial values of $\Delta\nu$ and $\epsilon_0$, for a suitable central radial order $n_0$ and a suitable range $\Delta k$. For each value of $\Delta\nu$ we determine the maximum $\mathcal{F}_{\max}(\Delta\nu)$ of $\mathcal{F}(\Delta\nu, \epsilon_0)$ as a function of $\epsilon_0$. This defines what we call *the matched filter response* as a function of $\Delta\nu$. Note that the procedure essentially determines the almost uniform separation of $\Delta\nu/2$ between the nearly degenerate peaks corresponding to even and odd degrees (this will be plotted transformed to $\Delta\nu$). In our analysis, we varied $\epsilon_0$ between 1.0 and 1.5 (typical values found from stellar models), and took $\Delta k = 5$, to include a total of 11 peaks in the analysis. The result of using trial values for the large separation between 40 and 120 $\mu$Hz is shown in Figure 11, for $n_0 = 19.5$, 20, 20.5, 21, and 21.5. The maximum matched filter response is found at 83.60 $\mu$Hz and clearly does not depend on $n_0$ within the range used. Note that sampling the spectrum at a frequency separation of $\Delta\nu/2$, and over a fixed range of radial orders, leads to a single peak in the response, unlike other types of comb analysis.

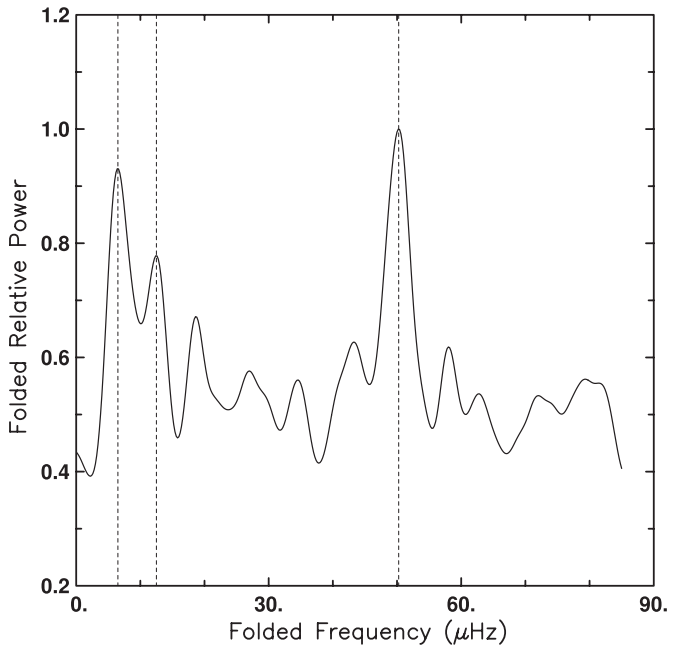


**Figure 12.** Power spectrum of Figure 9 after smoothing by 3 $\mu$Hz (FWHM) and averaging over successive slices of 83.5 $\mu$Hz over the domain of 1.2–2.4 mHz. The dashed lines indicate features which left to right correspond to modes of $l = 2$, 0, and 1, respectively.

The results shown in Figure 11 yielding $\Delta\nu_0 \approx 83.6\,\mu$Hz are stable and robust. In particular, the same value of the large separation can also be found by considering only the first, middle, or last half of the data sets, and it also continues to be seen if the strongest peak in the power spectrum at 1721.2 $\mu$Hz is arbitrarily set to zero. Thus, the 9.7 days of *HST* observations of HD 17156 with FGS2r have provided a secure detection of solar-like $p$ modes. Further quantification and use of the large separation follows below.

The next stage in the analysis attempts to fix further details of the oscillation frequencies. A goal here is to determine the small separation, which would provide constraints on the stellar age if possible, and to provide individual frequencies for as many modes as possible. A necessary associated goal will be to determine mode identifications, i.e., corresponding $n$ and $l$ with specific frequencies.

Figure 12 shows the result of folding the amplitude spectrum at 83.5 $\mu$Hz (taking into account the 83.44 $\mu$Hz splitting from fits to individual mode frequencies below) over the range of 1.2–2.4 mHz. The presence of strong contrast in this figure is simply another way of demonstrating that 83.5 $\mu$Hz is the correct large separation, e.g., folds at other values would show less contrast similar to the fall-off in distribution of the matched-filter response function of Figure 11 away from 83.5 $\mu$Hz. The expectation is that modes of $l = 0$, 1, and 2 only will be visible, with the modes at $l = 0$, and 2 nearly degenerate except for the small separation term of Equation (2). This leads to the expectation that a single isolated peak in this figure will correspond to $l = 1$, while a doubled peak with frequencies differing by much less than the large separation will represent the $l = 0$ and 2 modes. Guidance from theoretical models to be further discussed in Section 5 has led to the identification of modes provided in the caption to Figure 12 and in Table 1.

One might also expect to have a higher signal from the $l = 0$ modes than from the $l = 2$ modes in Figure 12 which is not the case. Kjeldsen et al. (2008b) give amplitude ratios of $l = 2/0$ for the Sun as 0.81, 0.75, and 0.67 at wavelengths of 402, 500, and 862 nm, respectively, which for the flux weighted centroid of these FGS observations at about 550 nm implies an expected ratio of 0.74. It might also be expected that the number of $l = 0$ modes detected would exceed $l = 2$; again this is not the case. In fact, due to the stochastic nature of the excitation it would not be surprising for modes with $l = 2$ sometimes to exceed the $l = 0$ mean amplitudes. Of the three stars with high S/N oscillations discussed in Chaplin et al. (2010), KIC 3656476 has a $\Delta\nu$ nearest HD 17156 and it shows equal numbers of detected $l = 0$ and 2 modes, and in two of the four jointly highest pairs of these the $l = 2$ amplitudes are larger than $l = 0$.

**Table 1**
Individual Frequencies ($\mu$Hz) Identified for HD 17156

| $n$ | $l = 0$ | $l = 1$ | $l = 2$ |
|---|---|---|---|
| 13 | ··· | ··· | $1258.2 \pm 1.4$ |
| 17 | $1516.0 \pm 1.4$ | ··· | ··· |
| 19 | ··· | $1721.2 \pm 0.9$ | $1759.4 \pm 1.4$ |
| 21 | ··· | $1885.4 \pm 1.3$ | ··· |
| 22 | $1932.3 \pm 1.2$ | $1970.4 \pm 1.5$ | ··· |
| 24 | ··· | ··· | $2177.9 \pm 1.3$ |

**Note.** Frequencies in $\mu$Hz of individual modes identified in HD 17156.

Table 1 provides the individual frequencies that follow from identifying the 10 highest peaks in the power spectrum. These all have an S/N in excess of 4 in the power spectrum of Figure 9. From the asymptotic relation, we identify 8 of the 10 highest frequencies. Their degree and order are shown in Table 1. The errors in Table 1 are estimated from simulations of the time series. We created a large number of stochastically excited modes with a mode lifetime of 3 days (similar to the lifetime of modes in the Sun) and estimated the accuracy with which we could detect the frequencies (taking peak amplitudes at the same S/N as in the present data) in a time series with the same sampling as the present data. A lifetime longer than 3 days would have resulted in smaller estimated frequency errors than indicated, while the errors would be larger if the mode lifetime is shorter than 3 days. The identification of the eight frequencies that fit the comb structure should not be seen as an unbiased frequency identification since it relies on selection of the modes that fit the comb structure for $l = 0$, 1, and 2. We also assume the existence of the asymptotic relation and the structure of stellar model frequencies to fix the identification. Another possible approach would be to use a wider frequency range when identifying the modes or use modes with lower amplitude. We have tried to use more modes and the fit to the stellar models does not depend (within the error bars) on the exact number of peaks included in the analysis. In the end we decided to use the 10 strongest peaks as a way to ensure that we only work with the most significant peaks and of those 10, 8 peaks agreed with the asymptotic relation corresponding to the comb power in Figure 12.

We have carried out a weighted least-squares fit of the asymptotic relation, Equation (2), to the eight identified frequencies, estimating the errors in coefficients from a Monte Carlo simulation. The resulting coefficients are: $\Delta\nu_0 = 83.44 \pm 0.15\,\mu$Hz, $D_0 = 0.90 \pm 0.19\,\mu$Hz, and the surface term $\epsilon = 1.15 \pm 0.04$.

Figure 13 shows the power spectrum from Figure 9 after smoothing with a Gaussian of FWHM = 3 $\mu$Hz on which the

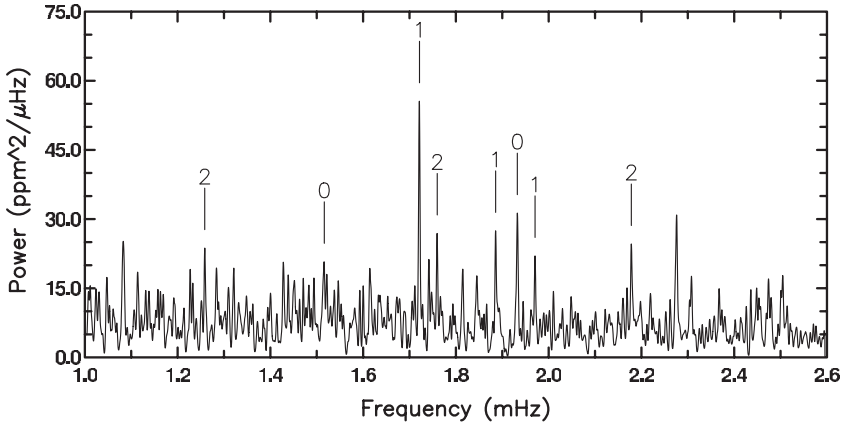


**Figure 13.** Version of power spectrum as in Figure 9 after a Gaussian smoothing of 3 $\mu$Hz FWHM has been applied. Frequencies of individual modes as listed in Table 1 are indicated with vertical bars at the listed frequency. The numerical label of 0, 1, or 2 provides the $l$ value.

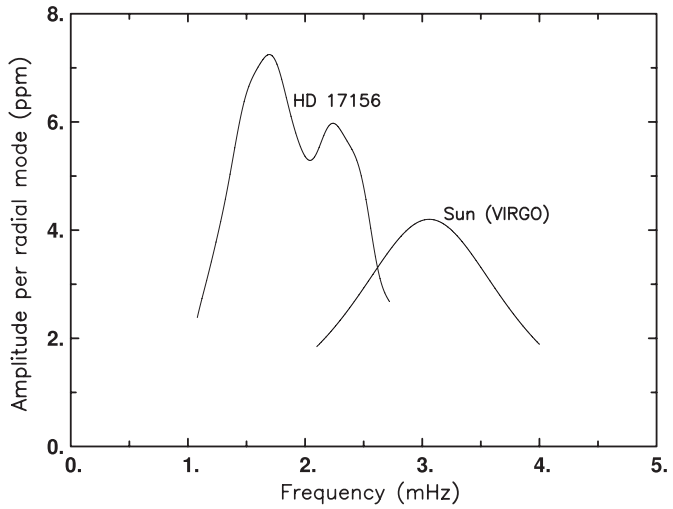


**Figure 14.** Amplitude per radial mode distribution for HD 17156 contrasted to that for the Sun. See the text for discussion.

individual mode frequencies of Table 1 are included. Over the frequency range 1.2–2.5 mHz, 8 of the 10 highest peaks are flagged as identified.

The final step in direct analyses of the amplitude spectrum is to assess the amplitude per mode from a smoothed power spectrum, and distribution of amplitudes with frequency following the method described in Kjeldsen et al. (2008b) and Huber et al. (2009). Converting the smoothed power spectrum (Figure 10) to power density by multiplying by the effective length of the observing run followed by fitting and subtracting the background noise and then multiplying by the large separation divided by the number of $p$ modes peaks per radial order scaled to the sensitivity of radial modes we may calculate the mean power per radial mode. The square root is then taken in order to convert to amplitude per oscillation mode (radial modes). The peak amplitude is about 7 ppm for $l = 0$, quite consistent with pre-observation estimates made using the published stellar parameters and Kjeldsen & Bedding (1995). The distribution of amplitudes for radial modes in HD 17156 is contrasted to those in the Sun in Figure 14. The extended, non-Gaussian distribution of amplitudes, albeit not well determined here, is similar to those found for Procyon (Arentoft et al. 2008).

## 5. STELLAR EVOLUTION MODELS AND INTERPRETATIONS

### 5.1. ASTEC–ADIPLS Analyses

The stellar evolution models are based on ASTEC (Christensen-Dalsgaard 2008a) and the associated eigenfrequency analysis code ADIPLS (Christensen-Dalsgaard 2008b). Briefly, the models use the OPAL equation of state (Rogers et al. 1996) and opacities (Iglesias & Rogers 1996), and the NACRE nuclear parameters (Angulo et al. 1999). The temperature gradient in the convection zone was computed using the Böhm-Vitense (1958) mixing-length treatment, with a mixing length of $\alpha_{\rm ML} = 2.00$ pressure scale heights, roughly calibrated to the corresponding solar models. In some cases convective core overshoot was included, over a distance of $\alpha_{\rm ov}$ min($r_{\rm cc}$, $H_p$), where $r_{\rm cc}$ is the radius of the convectively unstable region and $H_p$ is the pressure scale height at this point; the overshoot region was assumed to be fully mixed and adiabatically stratified. Diffusion and settling of helium were treated according to the simplified formulation of Michaud & Proffitt (1993). It was assumed that the initial abundances $X$ and $Z$ by mass of hydrogen and helium were related by $X = 0.77 - 3Z$, corresponding to a galactic enrichment $\Delta Y$ of helium determined by $\Delta Y = 2Z$; the values of $X$ and $Z$ were characterized by the observed [Fe/H], assuming a present solar surface composition with $Z/X = 0.0253$.

Evolution tracks have been computed to match the classical observed parameters as given in Fischer et al. (2007) and Ammler-von Eiff et al. (2009), leading to $T_{\rm eff} = 6082 \pm 60$ K and [Fe/H] $= 0.24 \pm 0.03$. A grid of models was computed, varying the mass between 1.26 and 1.33 $M_\odot$ in steps of 0.01 $M_\odot$, with composition, characterized by $Z$, corresponding to [Fe/H] varying between 0.18 and 0.30 in steps of 0.02, and with $\alpha_{\rm ov} = 0$, 0.05, and 0.1. All models included diffusion and settling of helium. Figure 15 shows the theoretical HR diagram with selected evolutionary tracks. The associated Table 2 lists the models along the evolutionary tracks at which the computed eigenfrequencies best match the observed frequencies (see Section 5.2).

### 5.2. Fitting the Observed Quantities

We have carried out least-squares fits of the observed frequencies in Table 1 and the observed effective temperature to the computed grid of models. For each model in the grid we computed the mean square difference of the model frequencies

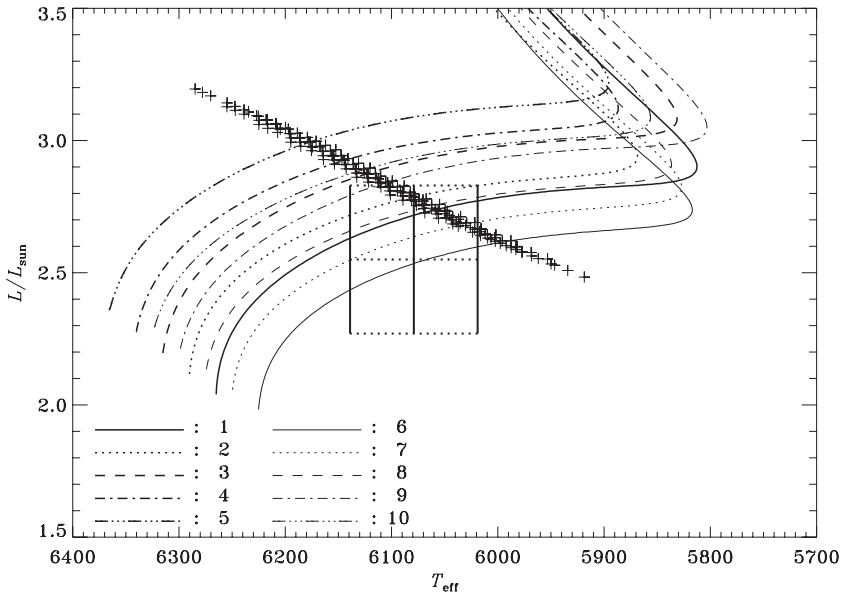


**Figure 15.** Theoretical H-R diagram with selected evolutionary tracks, corresponding to the models defined in Table 2. The "+" indicate the models along the full set of evolutionary sequences minimizing the difference between the computed and observed frequencies. The box is centered on the $L$ and $T_{\rm eff}$ as given in Winn et al. (2009), with a size matching the errors on these quantities ($T_{\rm eff}$ error from Table 3; $L$ from Winn et al. 2009).

**Table 2**
Stellar Evolution Models Fitting the Observed Frequencies in Table 1

| No. | $M_*/M_\odot$ | Age (Gyr) | $Z_0$ | $X_0$ | $R_*/R_\odot$ | $\langle\rho_*\rangle$ (g cm$^{-3}$) | $T_{\rm eff}$ (K) | $L_*/L_\odot$ | $\chi^2_\nu$ | $\chi^2$ |
|---|---|---|---|---|---|---|---|---|---|---|
| 1[a] | 1.28 | 2.936 | 0.0299 | 0.6803 | 1.505 | 0.5292 | 6058 | 2.74 | 2.46 | 2.57 |
| 2 | 1.29 | 2.756 | 0.0299 | 0.6803 | 1.508 | 0.5301 | 6079 | 2.79 | 2.43 | 2.43 |
| 3[a] | 1.30 | 2.557 | 0.0299 | 0.6803 | 1.509 | 0.5325 | 6123 | 2.87 | 2.59 | 3.14 |
| 4 | 1.31 | 2.389 | 0.0299 | 0.6803 | 1.512 | 0.5337 | 6144 | 2.93 | 2.65 | 3.85 |
| 5 | 1.32 | 2.215 | 0.0299 | 0.6803 | 1.514 | 0.5357 | 6176 | 2.99 | 2.82 | 5.47 |
| 6 | 1.28 | 3.069 | 0.0338 | 0.6687 | 1.507 | 0.5264 | 5987 | 2.62 | 2.48 | 4.80 |
| 7 | 1.29 | 2.865 | 0.0338 | 0.6687 | 1.510 | 0.5279 | 6021 | 2.69 | 2.40 | 3.31 |
| 8 | 1.30 | 2.670 | 0.0338 | 0.6687 | 1.512 | 0.5294 | 6054 | 2.76 | 2.34 | 2.51 |
| 9[a] | 1.31 | 2.474 | 0.0338 | 0.6687 | 1.514 | 0.5316 | 6099 | 2.85 | 2.52 | 2.64 |
| 10 | 1.32 | 2.307 | 0.0338 | 0.6687 | 1.517 | 0.5329 | 6120 | 2.90 | 2.56 | 3.03 |

**Notes.** Models minimizing $\chi^2_\nu$ (cf. Equation (5)) along the evolution tracks illustrated in Figure 15. The smallest value of $\chi^2_\nu$ is obtained for model 8. Models are shown for two values of the initial heavy-element and hydrogen abundances $Z_0$ and $X_0$, corresponding to [Fe/H] = 0.24 and 0.30. Models indicated by superscript "a" were computed with overshoot with $\alpha_{\rm ov} = 0.05$, the remaining models had no overshoot.

$\nu^{(\rm mod)}_{nl}$ from the observed frequencies $\nu^{(\rm obs)}_{nl}$:

$$\chi^2_\nu = \frac{1}{N-1}\sum_{nl}\left(\frac{\nu^{(\rm obs)}_{nl}-\nu^{(\rm mod)}_{nl}}{\sigma(\nu_{nl})}\right)^2 , \qquad (5)$$

where $N = 8$ is the number of observed frequencies and $\sigma(\nu_{nl})$ is the estimated error in the frequencies. This was minimized along each evolution track, characterized by the parameters $\{M, Z, \alpha_{\rm ov}\}$. We first determined the model, $\mathcal{M}_{\rm min}$, in the evolution sequence with the smallest value of $\chi^2_\nu$. We then assumed that the best-fitting model for these parameters could be obtained from the frequencies $\nu^{(\rm mod)}_{nl}(\mathcal{M}_{\rm min})$ by scaling,

$$\nu^{(\rm mod)}_{nl} = r\,\nu^{(\rm mod)}_{nl}(\mathcal{M}_{\rm min}) , \qquad (6)$$

and determined $r$ by minimizing $\chi^2_\nu$. The results presented in the following are based on these resulting minimal $\chi^2_\nu$ along the evolution tracks. According to Equation (3) the value of $r$ so obtained determines the radius of the best-fitting model as $R = r^{-2/3}R(\mathcal{M}_{\rm min})$; the remaining model quantities, including the effective temperature $T^{(\rm mod)}_{\rm eff}$, were then determined by linear interpolation in radius to this value. Finally, the departure from the observed effective temperature $T^{(\rm obs)}_{\rm eff}$ was included in the final

$$\chi^2 = \chi^2_\nu + \left(\frac{T^{(\rm obs)}_{\rm eff}-T^{(\rm mod)}_{\rm eff}}{\sigma(T_{\rm eff})}\right)^2 , \qquad (7)$$

where $\sigma(T_{\rm eff})$ is the standard error on the effective temperature.

The results of these fits are illustrated in Figure 16. A key goal of this analysis is to determine the mean stellar density $\langle\rho_*\rangle$ of the star; thus panels (a) and (b) show $\chi^2_\nu$ and $\chi^2$ against $\langle\rho_*\rangle$ for all the models in the grid. It is evident that minimizing $\chi^2_\nu$ along the evolution tracks leads to a narrow range of mean density, with well-defined minima at fixed $\alpha_{\rm ov}$. It is interesting that some preference is found for models without overshoot, although the difference between the three cases is of limited significance. Including also the constraint of the observed $T_{\rm eff}$ (panel b) produces a well-defined minimum in $\chi^2$, shifted toward slightly

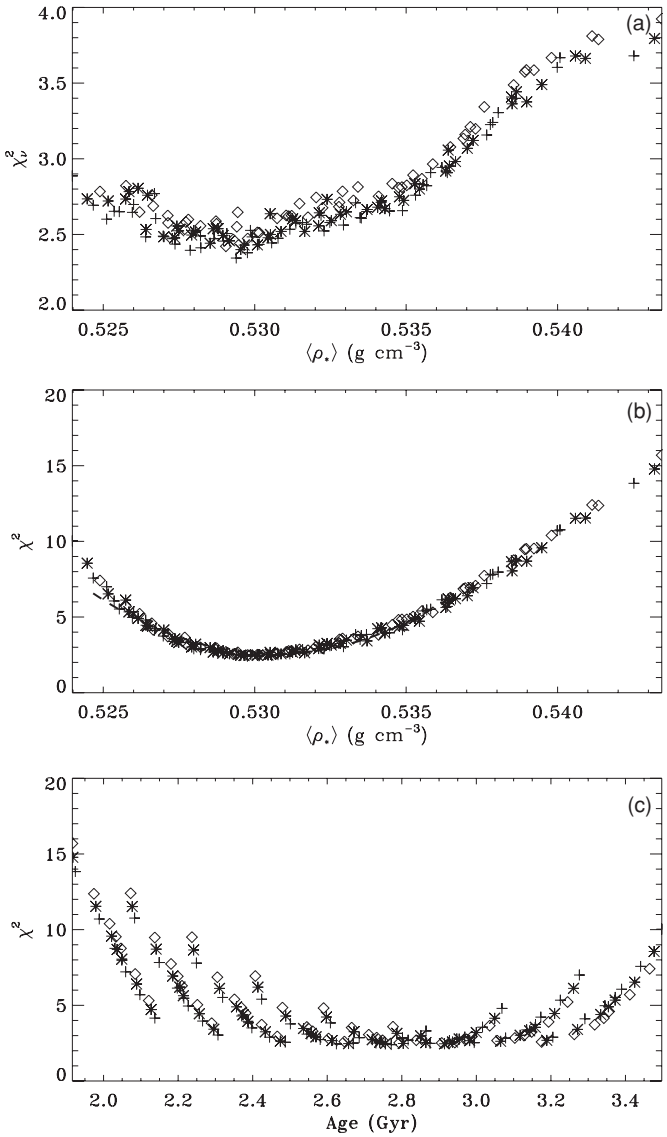


**Figure 16.** Results of fitting the observed frequencies and effective temperature to the grid of stellar models (see the text for details). Pluses, stars, and diamonds correspond to models with $\alpha_{ov} = 0$ (no overshoot), 0.05, and 0.1, respectively. Panel (a) shows the minimum mean square deviation $\chi^2_\nu$ of the frequencies (cf. Equation (5)) along each evolution track, against the mean density $\langle\rho_*\rangle$ of the corresponding models. Panel (b) similarly shows the combined $\chi^2$ (cf. Equation (7)); here the dashed curve is a parabolic fit to those points that have $\chi^2 \leqslant 7.2$ (see the text). Finally, panel (c) shows $\chi^2$ against the age for the models that minimize $\chi^2_\nu$; the different ridges correspond to the different masses in the grid, the more massive models resulting in a lower estimate of the age.

higher $\langle\rho_*\rangle$. To quantify the location and width of this minimum we have fitted a parabola to those points that have $\chi^2 \leqslant 3\chi^2_{\rm min}$, where $\chi^2_{\rm min} = 2.40$ is the minimum over all the sequences in the grid. This parabola has a minimum at $\langle\rho_*\rangle = 0.5301$ g cm$^{-3}$, and indicates a standard error in $\langle\rho_*\rangle$ of 0.0031 g cm$^{-3}$. Augmenting that by a factor of $\sqrt{2}$ to account for further possible systematic errors we arrive at our final estimate:

$$\langle\rho_*\rangle = 0.5301 \pm 0.0044\,{\rm g\,cm^{-3}}\ . \qquad (8)$$

The error estimate in Equation (8) is derived from the curvature of the $\chi^2$ surface. This estimate may also be cast in the form of a confidence interval in the manner described by, e.g., Kallinger et al. (2010). This is done by computing the relative probability $\exp^{-\chi^2/2}$ for each model, and then normalizing

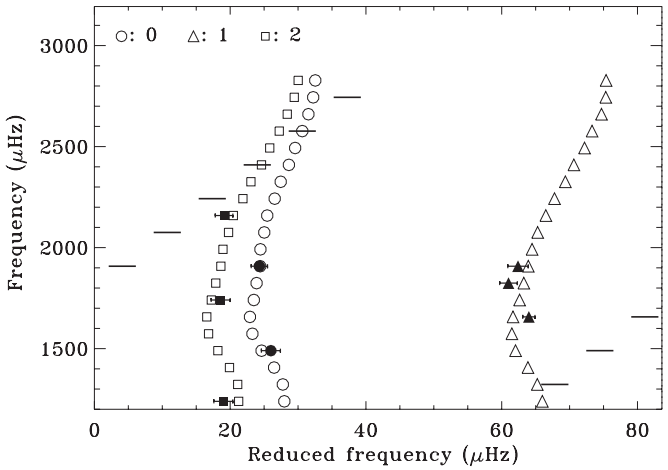


**Figure 17.** Asteroseismic échelle diagram comparing the observed frequencies of Table 1 (filled symbols with $1\sigma$ error bars) with values from the theoretical model minimizing $\chi^2_\nu$ (cf. Equation (5); open symbols); the model (model No. 8 in Table 2) has a mass $M = 1.30\,M_\odot$, [Fe/H] = 0.30 and an age of 2.67 Gyr. The horizontal axis shows frequency distribution within successive 83.6 $\mu$Hz slices, starting at a frequency of 68.8 $\mu$Hz, while the vertical axis shows the starting frequencies of the slices. The short horizontal lines indicate the frequency intervals where the response function drops below 50% due to orbital filtering (cf. Figure 9).

so that the sum of the probabilities over all models is unity. The desired confidence interval is then obtained by forming the marginal distribution of these probabilities with respect to the stellar mean density, and determining the range of densities that contain the desired fraction of the total probability. In the current case, $\chi^2$ as a function of $\langle\rho_*\rangle$ is very well approximated by a parabola; as a result, the marginal probability distribution is almost indistinguishable from a Gaussian, and the 68% confidence interval agrees closely with the standard error in $\langle\rho_*\rangle$ of 0.0031 g cm$^{-3}$ given above.

As illustrated in Figure 16(c) the fit also provides a constraint on the stellar age, although substantially affected by the spread in the mass in the grid, producing a broad nearly flat minimum in $\chi^2$. On the basis of the plot we estimate the age as $2.8 \pm 0.6$ Gyr.

In Figure 15, we have indicated the models minimizing $\chi^2_\nu$ for all the parameter sets in the grid. These clearly fall in a tightly confined region in the diagram, corresponding to the strongly constrained mean density. In order to further illustrate the properties of the fit we have considered models with masses between 1.28 and 1.32 $M_\odot$ and $Z = 0.0299$ ([Fe/H] = 0.24) and 0.0338 ([Fe/H] = 0.30), the latter case including the model minimizing $\chi^2_\nu$. For each pair $(M, Z)$ we selected the sequence leading to the smallest $\chi^2_\nu$. These are the evolution tracks plotted in Figure 15 and with properties listed in Table 2.

To illustrate the quality of the fit of the computed frequencies to the observations, Figure 17 compares the observed and computed frequencies in an *échelle diagram* (Grec et al. 1983, see caption), for the model in the grid which minimizes $\chi^2_\nu$. It is evident that the fit is excellent.

As an alternative fit to the model grid, which is independent of the individual frequencies, we have selected, on each evolution track, the model that matches the large separation $\Delta\nu$. Averaging the resulting mean densities over those models where $T_{\rm eff}$ differs by less than $2\sigma$ from the observed value yields $\langle\rho_*\rangle = 0.5290 \pm 0.0030$ g cm$^{-3}$, fully consistent with the more detailed fit.

We finally note that a potential problem in fitting solar-like oscillations is the effect of the near-surface layers on the

frequencies which is not properly taken into account in the adiabatic modeling considered here. This effect is well known in the analysis of helioseismic data (e.g., Christensen-Dalsgaard et al. 1996), where it can be isolated, owing to the availability of modes over a broad range of degrees. Kjeldsen et al. (2008a) suggested a procedure to eliminate the effect in the analysis of asteroseismic data by assuming a similar functional form as in the solar case, but a potentially different amplitude, to be determined as part of the fit; in addition, the procedure results in an estimate of the mean density of the star, through scaling from a suitable reference model. We have applied this to the observed frequencies in Table 1; this resulted in insignificant changes to the obtained fits and stellar parameters.

### 5.3. Comparing Asteroseismic and Planet-transit Mean Densities with Surface Gravity

Asteroseismology, and transit light curve modeling when very precise relative photometry is available, can both provide very precise (even accurate) determinations of the mean stellar density of stars. Since density is a simple function of stellar mass and radius, both asteroseismology and transit light curve modeling tightly constrain allowed choices of mass and radius in individual cases. However, arriving at unique estimates of the stellar mass and radius separately, as for example are needed if one wishes to use these to provide optimal estimates of the mass and radius of hosted planets as needed to advance and challenge the theoretical study of extrasolar planet formation and evolution, requires independent input.

For both asteroseismology and transit light curve modeling the classical approach to fixing the stellar mass and radius independently, given a measured stellar density, relies on stellar evolution models that best match observed constraints, typically some combination of temperature, metallicity, and surface gravity (luminosity in our case with the known parallax, although we use luminosity only as a consistency check), hence bringing in inferences from spectroscopy. Accurate estimates of stellar masses and radii then depend on correct models of both stellar evolution and stellar atmospheres. How good are these? Figure 18 illustrates one outstanding issue, that may perhaps exist primarily for stars in the high metallicity domain, as is the case for HD 17156, and for many exoplanet hosts given the strong correlation of high metallicity and existence of such planets (Fischer & Valenti 2005; Valenti & Fischer 2005). Spectroscopic studies have fixed $\log(g)$ to be $4.29 \pm 0.06$ (Fischer et al. 2007) and $4.33 \pm 0.05$ (Ammler-von Eiff et al. 2009), with very consistent determinations of $T_{\rm eff}$ and [Fe/H] between the two independent studies as well; see Table 3 for summaries. In Figure 18, we show the range of stellar masses and radii that jointly meet either the asteroseismic constraint for HD 17156 where $M/R^3$ is a constant, or the constraint imposed by published spectroscopic $\log(g)$ values which requires $M/R^2$ to be a constant. In this diagram an ideal result would be that the two sets of joint $M$, $R$ constraints cross at the location of the preferred values obtained from other considerations. Instead, we are left with the result that there is no agreement, the asteroseismic result for radius remains nearly $3\sigma$ away from the $\log(g)$ constraint near the preferred mass. Note that the transit light curve analyses of Nutzman et al. (2011) also impose a constraint with the functional form of that from asteroseismology, in relative terms this would have a central value that falls near, but slightly above, the preferred asteroseismic value, with error offsets about five times larger than those shown by asteroseismology. Clearly, the spectroscopic $\log(g)$ of 4.31 is well above

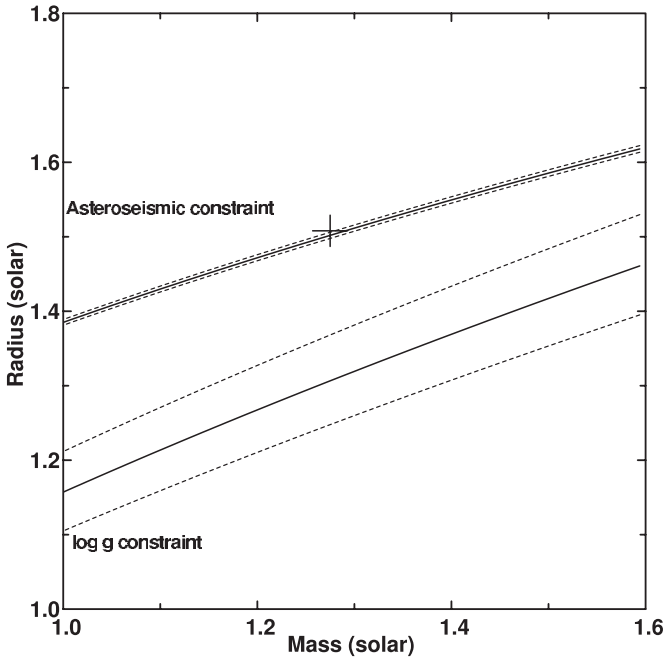


**Figure 18.** Upper curves show the allowed $M_*$, $R_*$ values that satisfy the asteroseismology large separation constraint (solid curve preferred value of $\langle\rho_*\rangle = 0.5301\,{\rm g\,cm^{-3}}$, dashed lines the 0.0044 error offsets from this). The lower curves show the corresponding values that satisfy the spectroscopic $\log(g)$ value of 4.31, with solid and dashed curves preferred and 0.04 error offsets. The large plus symbol shows the preferred value of $M_*$, $R_*$, and allowed error range resulting from the transit light curves analyses (Nutzman et al. 2011)—note the excellent consistency with asteroseismology.

the asteroseismic (or transit light curve) value of about 4.19 for HD 17156. Perhaps in the high metallicity domain of interest for HD 17156, and many exoplanet hosts, the stronger lines result in biases for $\log(g)$.

### 5.4. Calibration of Stellar Mass and Radius to Eclipsing Binaries

Figure 18 shows that radius estimates based on spectroscopic $\log(g)$ determinations are problematic at the 10% level, whereas estimates based on transit timing and on asteroseismology are mutually consistent. This consistency provides a necessary, but not sufficient, condition for using the stellar mean density as measured from transit light curves or from asteroseismology to provide the truly desired stellar masses and radii. To verify that we can combine a mean density measurement with stellar evolution models to obtain accurate masses and radii, we must test our techniques against stars for which there are accurate and independent measures of mass and radius. Eclipsing binaries (EBs) comprise the only large set of stars for which such information exists. The mass and radius estimates derived from light curve and radial velocity measurements of EBs are almost independent of theory, and in many cases accuracies of better than 3% can be obtained for both quantities. Torres et al. (2009) have recently published the fundamental data for all known EBs meeting this standard of accuracy, a list containing 190 stars. Brown (2010) applied the mean-density analysis to 156 of these (all with masses $M_*$ satisfying $0.4\,M_\odot \leqslant M_* \leqslant 5\,M_\odot$), matching Yonsei–Yale (YY) models (Yi et al. 2001) to observational estimates of mean density, effective temperature, and metallicity. Comparing radii and masses from model matching to those measured directly showed that matching the YY models generally yielded accurate results, with systematic errors estimated

**Table 3**
System Parameters of HD 17156

| Parameter | Value | $1\sigma$ Limits | Comment |
|---|---|---|---|
| Mean density, $\langle\rho_*\rangle$ (g cm$^{-3}$) | 0.5301 | ±0.0044 | A |
| Age (Gyr) | 2.8 | ±0.6 | A |
| Effective temp, $T_{\rm eff}$(K) | 6082 | ±60 | B |
| Surface gravity, log($g$) (cgs) | 4.31 | ±0.04 | B |
| Metallicity, [Fe/H]* | 0.24 | ±0.03 | B |
| Mass, $M_*$ ($M_\odot$) | 1.285 | ±0.026 | C |
| Radius, $R_*$ ($R_\odot$) | 1.507 | ±0.012 | C |
| Age (Gyr) | 3.2 | ±0.3 | C |
| Luminosity, $L_*$ ($L_\odot$) | 2.79 | ±0.14 | D |
| Surface gravity, log($g$) (cgs) | 4.191 | ±0.004 | D |

**Notes.** (A) Based on asteroseismic analysis of this paper. (B) Spectroscopic results averaging from Fischer et al. (2007) and Ammler-von Eiff et al. (2009). * For the purposes of deriving MCMC-based errors (Brown 2010) on $M_*$ and $R_*$, we have adopted a doubling of the [Fe/H] error to ±0.06. (C) Function of A and B parameters and use of stellar evolution models. (D) Derived from B and C parameters.

to be smaller than 2% in radius and 6% in mass. Larger errors can occur for cool and rapidly rotating stars, in which surface magnetic activity is thought to interfere with convective energy transport, leading to radii that are larger than the YY models predict. HD 17156 is, however, a slow rotator that is somewhat hotter than the Sun. For this star, systematic errors resulting from activity should be small, certainly less than 1% based on the expected rotation period of 19 days mentioned in Section 2, and the lack of any photometric variations in excess of ∼0.1% intrinsic to the star in our FGS photometry.

### 5.5. Stellar Parameters from the Inferred Mean Density

To obtain an independent estimate of the values of the basic stellar parameters and their errors, we have carried out a Markov Chain Monte Carlo (MCMC) fit of stellar models to the observed $T_{\rm eff}$ and [Fe/H] and the asteroseismically inferred $\langle\rho_*\rangle$ (see Brown 2010 for details). The models were obtained from the YY compilation (Yi et al. 2001). As for the ASTEC models used in the asteroseismic analysis the YY models use OPAL opacities and equation of state and include diffusion and settling of helium, although with a somewhat different formulation. Core overshoot is included, with a step-function dependence of overshoot distance on stellar mass (see Demarque et al. 2004 for details), such that for the models relevant to the present fits $\alpha_{\rm ov}$ is probably generally equal to 0.1.

The inferred parameters are listed in Table 3. The mass, radius, and luminosity are very close to the values obtained from the asteroseismic analysis (see Table 2). The age inferred from the MCMC analysis, $3.2 \pm 0.3$ Gyr, is formally consistent with the asteroseismic value. However, the difference of 0.4 Gyr probably reflects systematic differences between the ASTEC and YY evolution codes. This deserves further investigation.

## 6. DISCUSSION

### 6.1. Summary and Comparison with Previous Results

We reported the detection of the asteroseismic large separation for HD 17156, and determined the mean stellar density resulting from this to be $0.5301 \pm 0.0044$ g cm$^{-3}$. The best determination before these observations comes from Winn et al. (2009) who relied on ground-based transit light curve analysis to fix $\langle\rho_*\rangle$ at the $1\sigma$ range of 0.486–0.655 g cm$^{-3}$, with a preferred value of 0.589 g cm$^{-3}$. Our density is significantly different than the Winn et al. (2009) value, but well within their original confidence range.

### 6.2. Comparison with Joint HST FGS Transit Analysis

Of more relevance to comparing our asteroseismic results to those from transit light curve based studies are the results from independent *HST* FGS observations obtained as a part of this program. Nutzman et al. (2011) find a mean stellar density of $0.522^{+0.021}_{-0.018}$ g cm$^{-3}$. This transit-based determination is $1.8\sigma$ from the asteroseismic result, while the latter is only $0.4\sigma$ off from the transit analysis based on its larger error allowances. Clearly, of the two extreme outcomes possible from this first comparison of the two independent techniques that both yield what may be referred to as direct determinations of $\langle\rho_*\rangle$ we are firmly in the domain of mutual confirmation, rather than a potential domain of disagreement calling for further understanding of one or both techniques. As noted in Section 5.3, however, the same cannot be said for consistency with the spectroscopically determined log($g$) where there is a nearly $3\sigma$ discrepancy in the sense that the spectroscopic log($g$) is too large.

### 6.3. Future Prospects from Kepler

In the near future, the *Kepler* Mission may be expected to provide similar results in which both asteroseismology and transit light curve analysis will provide simultaneous constraints for the mean stellar density of planet host stars. The three previously known exoplanets in the *Kepler* field of view will be observed at short cadence (58.8 s) throughout the mission, thus supporting asteroseismology on these targets. "Only" 512 targets may be followed at short cadence at any time, the bulk of observations for over 150,000 stars with *Kepler* will use the long cadence of 29.4 minutes which suffices for detection of planets via transits. The *Kepler* throughput is a factor of about 5.9 higher than that for the *HST* FGS2r used for the observations in this paper, following from the use of back-side illuminated CCDs on *Kepler*, and a broad bandpass of roughly 420–880 nm, *despite the factor of 6.4 relative advantage in aperture area of HST compared to Kepler*. Furthermore, *Kepler* should reach a duty cycle of nearly 100% during the month-long observing blocks between short breaks for telemetering accumulated data to the ground, compared to the uniquely high 72.6% duty cycle reached with *HST* for this observation taking advantage of a CVZ passage. This results in a net advantage in terms of Poisson statistics limit of 2.27 mag for *Kepler* observations compared to those in this paper. What our *HST* observations have provided for a $V = 8.17$ star in 10 days should be possible with *Kepler* for a $V = 10.44$ mag star in the same length of time. Also weighing in favor of *Kepler* asteroseismology is an expected window function without the sidelobes resulting from the orbit of *HST* and the daily passages through the SAA. And of course it should be routine for *Kepler* to devote much longer observing periods to targets than was the case for this unusually long *HST* observation. The initial target catalog for *Kepler* long cadence observations contains about 2500 targets brighter than the level which should return Poisson limited precisions per unit time as good or better than those discussed in this paper. To reach the same S/N on expected oscillations in the three previously known exoplanet hosts within the *Kepler* field of view, as for these *HST* observations of HD 17156, should take about two months for TrES-2 at $V = 11.4$, 8 days for HAT-P-7 at $V = 10.5$, and

20 days for HAT-P-11 at $V = 9.6$ taking into account the expected oscillation properties of each.

Coming at a time of significant stress on the *HST* project these observations required the expert assistance of many individuals to develop and execute. Especially noteworthy were the skill and tireless efforts provided by Merle Reinhart at STScI in expertly crafting the Phase II program to use all available observing time in the orbits allocated, and the efforts from Mike Wenz at Goddard Space Flight Center for shepherding the proposal through pre-flight reviews and monitoring engineering performance during execution. We thank the STScI Director, Matt Mountain, for the generous DD time award that made these results possible. We thank Matt Holman and Jeff Valenti for discussion. Financial support for this work was provided through program GO/DD-11945 from STScI.

*Facility: HST* (FGS)

## REFERENCES

Ammler-von Eiff, M., Santos, N. C., Sousa, S. G., Fernandes, J., Guillot, T., Israelian, G., Mayor, M., & Melo, C. 2009, A&A, 507, 523
Angulo, C., et al. 1999, Nucl. Phys. A, 656, 3
Arentoft, T., et al. 2008, ApJ, 687, 1180
Barbieri, M., et al. 2007, A&A, 476, L13
Bean, J. L., et al. 2008, A&A, 486, 1039
Bedding, T. R., & Kjeldsen, H. 2008, in ASP Conf. Ser. 384, Proc. 14th Cambridge Workshop on Cool Stars, Stellar Systems, and the Sun, ed. G. van Belle (San Francisco, CA: ASP), 21
Böhm-Vitense, E. 1958, Z. Astrophys., 46, 108
Brown, T. M. 2010, ApJ, 709, 535
Brown, T. M., & Gilliland, R. L. 1994, ARA&A, 32, 37
Chaplin, W. J., et al. 2010, ApJ, 713, L169
Charbonneau, D., Brown, T. M., Latham, D. W., & Mayor, M. 2000, ApJ, 529, L45
Christensen-Dalsgaard, J. 2004, Sol. Phys., 220, 137
Christensen-Dalsgaard, J. 2008a, Ap&SS, 316, 13
Christensen-Dalsgaard, J. 2008b, Ap&SS, 316, 113
Christensen-Dalsgaard, J., Arentoft, T., Brown, T. M., Gilliland, R. L., Kjeldsen, H., Borucki, W. J., & Koch, D. 2007, Commun. Asteroseismol., 150, 350
Christensen-Dalsgaard, J., Arentoft, T., Brown, T. M., Gilliland, R. L., Kjeldsen, H., Borucki, W. J., & Koch, D. 2008, J. Phys.: Conf. Ser., 118, 12
Christensen-Dalsgaard, J., et al. 1996, Science, 272, 1286
Cochran, W. D., Redfield, S., Endl, M., & Cochran, A. L. 2008, ApJ, 683, L59
Demarque, P., Woo, J.-H., Kim, Y.-C., & Ki, S. K. 2004, ApJS, 155, 667
Fischer, D. A., & Valenti, J. 2005, ApJ, 622, 1102
Fischer, D. A., et al. 2007, ApJ, 669, 1336
Gilliland, R. L., Bohlin, R. C., McCullough, P. R., & Nelan, E. 2009, Instrument Science Report TEL 2009-01 (Baltimore, MD: STScI)
Gilliland, R. L., et al. 1993, AJ, 106, 2441
Grec, G., Fossat, E., & Pomerantz, M. 1983, Sol. Phys., 82, 55
Henry, G. W., Marcy, G. W., Butler, R. P., & Vogt, S. S. 2000, ApJ, 529, L41
Huber, D., Stello, D., Bedding, T. R., Chaplin, W. J., Arentoft, T., Quirion, P.-O., & Kjeldsen, H. 2009, Commun. Asteroseismol., 160, 74
Iglesias, C. A., & Rogers, F. J. 1996, ApJ, 464, 943
Kallinger, T., Gruberbauer, M., Guenther, D. B., Fossati, L., & Weiss, W. W. 2010, A&A, 510, 106
Kjeldsen, H., & Bedding, T. R. 1995, A&A, 293, 87
Kjeldsen, H., Bedding, T., & Christensen-Dalsgaard, J. 2008a, ApJ, 683, L175
Kjeldsen, H., et al. 2005, ApJ, 635, 1281
Kjeldsen, H., et al. 2008b, ApJ, 682, 1370
Michaud, G., & Proffitt, C. R. 1993, in IAU Colloq. 137, ASP Conf. Ser. 40, Inside the Stars, ed. A. Baglin, W. W. Weiss (San Francisco, CA: ASP), 246
Michel, E., et al. 2008, Science, 322, 558
Narita, N., et al. 2009, PASJ, 61, 991
Nelan, E. P., et al. 2008, FGS Instrument Handbook for Cycle 17 (Baltimore, MD: STScI)
Nutzman, P., et al. 2011, ApJ, 726, 3
Rogers, F. J., Swenson, F. J., & Iglesias, C. A. 1996, ApJ, 456, 902
Seager, S., & Mallén-Omelas, G. 2003, ApJ, 585, 1038
Sozzetti, A., Torres, G., Charbonneau, D., Latham, D. W., Holman, M. J., Winn, J. N., Laird, J. B., & O'Donovan, F. T. 2007, ApJ, 664, 1190
Torres, G., Andersen, J., & Gimenez, A. 2009, A&AR, 18, 67
van Leeuwen, F. (ed.) 2007, Astrophys. Space Sci. Libr. 350, *Hipparcos*, The New Reduction of the Raw Data (Dordrecht: Springer),
Valenti, J. A., & Fischer, D. A. 2005, ApJS, 159, 141
Winn, J. N. 2008, in IAU Symp. 253, Transiting Planets, ed. F. Pont, et al. (Cambridge: Cambridge Univ. Press),
Winn, J. N., et al. 2009, ApJ, 693, 794
Wittenmyer, R. A., et al. 2005, ApJ, 632, 1157
Yi, S., Demarque, P., Kim, Y.-C., Lee, Y.-W., Ree, C. H., Lejeune, T., & Barnes, S. 2001, ApJS, 136, 417